ARMY RESEARCH LABORATORY

CFD Prediction of Magnus Effect in Subsonic to Supersonic Flight

by James DeSpirito

ARL-TR-4929 **September 2009**

NOTICES

Disclaimers

The findings in this report are not to be construed as an official Department of the Army position unless so designated by other authorized documents.

Citation of manufacturer's or trade names does not constitute an official endorsement or approval of the use thereof.

Destroy this report when it is no longer needed. Do not return it to the originator.

Army Research Laboratory
Aberdeen Proving Ground, MD 21005-5066

ARL-TR-4929 **September 2009**

CFD Prediction of Magnus Effect in Subsonic to Supersonic Flight

James DeSpirito
Weapons and Materials Research Directorate, ARL

REPORT DOCUMENTATION PAGE	Form Approved OMB No. 0704-0188

1. REPORT DATE *(DD-MM-YYYY)*	2. REPORT TYPE	3. DATES COVERED (From - To)
September 2009	Final	September 2006–December 2007

4. TITLE AND SUBTITLE	5a. CONTRACT NUMBER
CFD Prediction of Magnus Effect in Subsonic to Supersonic Flight	5b. GRANT NUMBER
	5c. PROGRAM ELEMENT NUMBER

6. AUTHOR(S)	5d. PROJECT NUMBER
James DeSpirito	62618AH80
	5e. TASK NUMBER
	5f. WORK UNIT NUMBER

7. PERFORMING ORGANIZATION NAME(S) AND ADDRESS(ES)	8. PERFORMING ORGANIZATION REPORT NUMBER
U.S. Army Research Laboratory ATTN: RDRL-WMB-C Aberdeen Proving Ground, MD 21005-5066	ARL-TR-4929

9. SPONSORING/MONITORING AGENCY NAME(S) AND ADDRESS(ES)	10. SPONSOR/MONITOR'S ACRONYM(S)
	11. SPONSOR/MONITOR'S REPORT NUMBER(S)

12. DISTRIBUTION/AVAILABILITY STATEMENT

Approved for public release; distribution is unlimited.

13. SUPPLEMENTARY NOTES

14. ABSTRACT

The aerodynamic coefficients of the 7-cal. U.S. Army-Navy Spinner Rocket were characterized using computational fluid dynamic (CFD) calculations and validated using archival experimental data. The static aerodynamic coefficients, roll-damping, and pitch-damping moments were accurately predicted by steady-state Reynolds-averaged Navier-Stokes (RANS) as well as unsteady hybrid RANS/large-eddy simulation (LES) CFD. The Magnus moment was overpredicted in the subsonic and transonic regime. Unsteady RANS/LES computations did not improve the prediction of Magnus moment at the lower Mach numbers. Both steady-state RANS and unsteady RANS/LES simulations resulted in similar predictions of all aerodynamic coefficients. Distributions of Magnus moment along the projectile body showed that the largest difference in Magnus moment between configurations and Mach numbers was in the last caliber of the projectile body.

15. SUBJECT TERMS

computational fluid dynamics, pitch damping, Magnus, roll damping, aerodynamic

16. SECURITY CLASSIFICATION OF:			17. LIMITATION OF ABSTRACT	18. NUMBER OF PAGES	19a. NAME OF RESPONSIBLE PERSON
a. REPORT	b. ABSTRACT	c. THIS PAGE			James DeSpirito
Unclassified	Unclassified	Unclassified	UU	44	19b. TELEPHONE NUMBER (*Include area code*) 410-306-0778

Standard Form 298 (Rev. 8/98)
Prescribed by ANSI Std. Z39.18

Contents

List of Figures

List of Tables

Acknowledgments

The author thanks Dr. Paul Weinacht and Dr. Sidra Silton of the U.S. Army Research Laboratory (ARL) for many helpful discussions. This work was supported in part by a grant of high-performance computing time from the U.S. Department of Defense (DOD) High Performance Computing Modernization program at the ARL DOD Supercomputing Resource Center, Aberdeen Proving Ground, MD.

1. Introduction

The computation of Magnus effects via steady-state computational fluid dynamics (CFD) in the supersonic and transonic flight regimes was demonstrated more than 20 years ago (*1–3*). The comparisons with experimental data in the transonic region were limited and tended to consist of Mach numbers >1.0. Recent work (*4*) directly comparing time-accurate and steady-state methods to predict the Magnus moment in the supersonic regime shows each method accurate to within the error in the experimental data. Recent studies (*5–7*) using the much-improved meshes, turbulence models, and solver methodologies have shown that the prediction of Magnus moment near Mach 1.0 and below does not always compare well with experimental data. Silton (*5*) demonstrated limited success in predicting the Magnus moment of a 0.50-cal. (12.7-mm) projectile. The prediction of Magnus moment in the subsonic and supersonic regimes was found to be fair, but in the transonic regime it was not as good. Another study of the 25-mm M910 training projectile (*6*) predicted the static aeroballistic coefficients plus Magnus moment and roll-damping moment over the Mach number range of $0.4 < M < 4.5$. Magnus moment was predicted adequately via steady-state CFD for $M > 2$. However, for $M < 2$ the Magnus moment was overpredicted, not capturing the large negative values of nonlinear Magnus moment present in the M910 flight dynamics. Time-accurate, hybrid Reynolds-averaged Navier Stokes (RANS) and large-eddy simulation (LES) calculations appeared to perform better, accurately predicting the Magnus moment in the subsonic Mach number range. A more recent continuation of the M910 study (*7*), which used a more refined LES mesh in the wake region, again showed that time-accurate RANS/LES simulations performed better than steady-state computations in the subsonic range. However, the newer calculations did not predict the magnitude of the Magnus moment as well as in the earlier study (*6*).

Today, nonlinear Magnus moments are routinely observed for nearly all spin-stabilized projectiles at subsonic and transonic speeds (*8*). Observing the distribution of Magnus moment along the length of a typical spin-stabilized projectile shows that the nonlinearity is confined to very near the base of the projectile. The shape of the projectile base has a large effect on the nonlinear Magnus component (*4*). A rounded base was shown to exhibit a large variation with angle of attack, while a flat (sharp-cornered) base nearly eliminates the nonlinear Magnus effect. In the M910 study (*6, 7*), significant differences in the near-body wake of the projectile were observed between steady-state RANS and unsteady RANS/LES simulations at subsonic and transonic speeds. It was speculated that the unsteady base flow interacts with the asymmetric pressure distribution (which is responsible for the Magnus effect) on the projectile body. Some or all of this interaction effect is not captured by the steady-state simulations. The wake effects on the body forces are likely small enough not to significantly impact the normal force and pitching moment; however, the Magnus force is much smaller, and the small wake effect perturbations can significantly effect the Magnus moment.

Research in the area of base flow phenomena is ongoing. Other researchers have recently used unsteady RANS/LES methods to investigate projectile base flows in the supersonic (*9*) and subsonic and transonic regimes without (*10)* and with (*11*) spin. Their work primarily concentrates on the demonstration and validation of their hybrid RANS/LES technique and illustrates the unsteady quantities that can be obtained with the hybrid RANS/LES methods. The authors have not published work investigating nonzero angles of attack; thus no Magnus effects have been reported.

The capabilities of steady-state CFD to predict the static aerodynamic coefficients of munitions are well established. Roll damping and pitch damping have also been accurately predicted using steady-state CFD methods (*12*). The goal of this report is to further evaluate the steady-state RANS and unsteady RANS/LES CFD methods to predict the Magnus effects in the transonic and subsonic flight regimes. The accurate prediction of Magnus moment across the Mach number range is important because it, along with the other dynamic and static coefficients, is needed as input into trajectory codes for preliminary design purposes. If CFD can demonstrate high-confidence prediction of these dynamic coefficients, then it can be used with confidence to evaluate projectile designs in lieu of free-flight and spark range tests in the preliminary design phase. Full aerodynamic characterization using CFD, spark range, and wind tunnel investigations can then be performed on the final design concepts.

The projectile used in this study is the U.S. Army-Navy Spinner Rocket (ANSR), for which extensive archival experimental data exists (both free-flight spark range and wind tunnel) (*13–15*). As such, this model has also been used as a reference for many previous semi-empirical and CFD calculations. The basic interest of the ANSR test program was in the dynamic stability of spinning bodies of revolution. The two important ballistic coefficients for determining dynamic stability—Magnus and pitch-damping moments—are dependent on the center of gravity (c.g.). Therefore, three c.g. locations were investigated by using different materials for parts of the projectile body. In this report, the standard-base and boattail versions of the 7-cal.-long ANSR model are studied in the transonic and supersonic Mach regimes, $0.7 < M < 2.5$.

2. Numerical Approach

2.1 Computational Geometry and Mesh

Two different ANSR configurations were investigated, each with a total body length of 7 cal. (1 cal. = 20 mm). The computational models of the standard-base and boattail versions of the ANSR are shown in figure 1. Each consists of a 2-cal. secant ogive followed by a 5-cal. cylindrical afterbody. The boattail model had a 0.5-cal., 7° boattail. The three c.g. locations

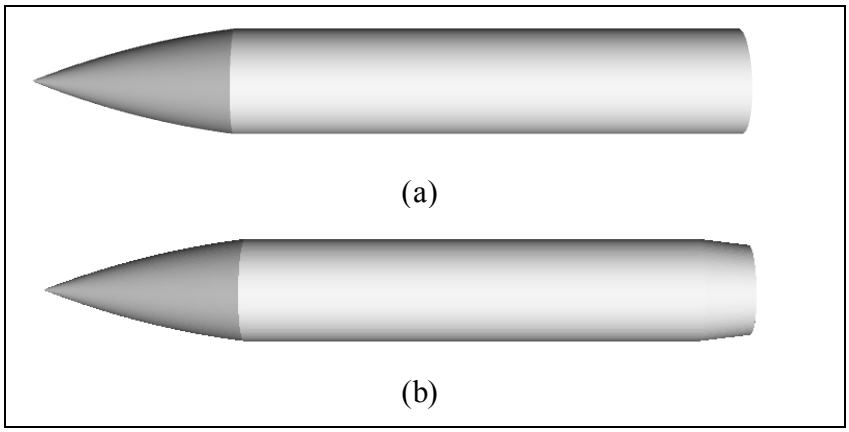

Figure 1. The 7-cal. Army-Navy Spinner Rocket (ANSR) model with (a) standard base and (b) 0.5-cal. boattail.

investigated in the experimental program were also studied here, 3.250, 4.036, and 4.818 cal. from the nose.

The geometry and unstructured mesh were generated using GAMBIT, a geometry and grid preprocessor supplied with the FLUENT CFD software suite (*16*). A full, three-dimensional (3-D) mesh was required to simulate the spinning shell at angle of attack. In generating the meshes, boundary layer mesh spacing was used near the projectile body. The meshes used in the study are summarized in table 1. Three versions of the same standard-base (SB) mesh were generated to use in a grid resolution study. The smaller standard base and boattail (BT) meshes (SB-1 and BT-1) were used for all the steady-state computations. The larger meshes (SB-2 and BT-2) were used for the unsteady RANS/LES computations, which require a denser mesh behind the projectile to resolve the large eddies in the wake. All the other mesh characteristics were the same. Table 1 shows the number of cells in the circumferential and axial directions along the projectile body, in the radial direction away from the body, and on the axis to the rear and forward of the body.

Table 1. Computational mesh characteristics of 7-cal. ANSR model.

Case	Number Cells	Number Circumferential Cells	Number Axial Cells	Number Radial Cells	Number Cells to Rear	Number Cells Forward
SB-1	3,455,920	144	170	106	210	102
SB-1a	1,781,200	112	136	84	168	82
SB-1b	5,878,112	176	200	116	252	122
BT-1	3,731,224	144	202	106	210	102
SB-2	11,296,728	144	170	106	492	102
BT-2	11,754,520	144	202	106	492	102

The extent of the computational domain was the same for all meshes: 50 cal. radially away, 35 cal. forward, and 50 cal. rearward of the projectile. The y^+ value was also the same for all meshes, 2.5×10^{-5}. The y^+ value is actually based on the first cell centroid, or one-half of the first-edge spacing. Resolving the viscous boundary layer is critical for predicting the Magnus and roll-damping moments; therefore, wall functions were not used. Equations were integrated to the wall instead. Normally, a y^+ value on the order of 1.0 is adequate to resolve the boundary layer. However, a y^+ value of 0.5 or less was needed to ensure capturing the Magnus effect of the spinning shell. All mesh stretching ratios were kept to 1.2 or less.

The mesh for steady-state RANS computations, SB-1, is shown in figure 2a. It is an unstructured mesh consisting of hexagonal cells, with 144 cells in the circumferential direction. An O-grid-type mesh was generated around the projectile body to contain the dense viscous mesh required to resolve the boundary layer. This O-grid extended to a distance of 0.1 cal. from the projectile body. A C-grid-type mesh was then generated around the body to a distance of 0.5 cal. from the projectile body. The C-grid mesh was extended from the base of the projectile to the rear boundary of the computational domain. The mesh stretching was kept very small behind the projectile to ensure the wake flow was resolved. The mesh stretching was about 1% for the first 3 cal., and then increased to about 4% from that point to the rear end of the computational domain. The region ahead of the projectile was meshed with a mapped-type mesh. The remainder of the computational domain was meshed with hexagons generated by revolving the paved quads around the axis (this is a Cooper mesh in GAMBIT). The mesh for the boattail ANSR, BT-1, was very similar to SB-1. Only the small region in the vicinity of the base was changed, with most of the mesh the same as the standard-base ANSR.

Two additional meshes based on SB-1 were generated as part of a grid convergence investigation. These are listed in table 1 as SB-1a and SB-1b, respectively. These meshes were made to be nominally one-half and twice the size, respectively, of SB-1. To achieve this, the number of cells in the axial and circumferential directions was divided by and multiplied by the $\sqrt[3]{2}$, respectively. However, in the radial direction, the first cell spacing was kept constant, and the number of cells was only reduced to the extent that the mesh stretching ratio did not exceed 1.25. If the mesh in the radial direction is reduced to a level that is inappropriate for resolving the viscous boundary layer, then the coarse mesh is almost guaranteed to produce poor results.

Although meshes SB-1 and BT-1 were designed for steady-state RANS simulations, the cell density in the wake region was made higher than might normally be used. This was done to see if unsteady RANS/LES simulations on this mesh could produce reasonable results, as they had in a previous study (*6*). However, two additional meshes, SB-2 and BT-2, were made with a dense mesh of nearly isotropic cells for about 0.75 body lengths behind the projectile. These meshes are more appropriate to capture the large-scale eddy structures in the LES (wake) region. A comparison of the mesh density in the wake between the RANS mesh and RANS/LES mesh for

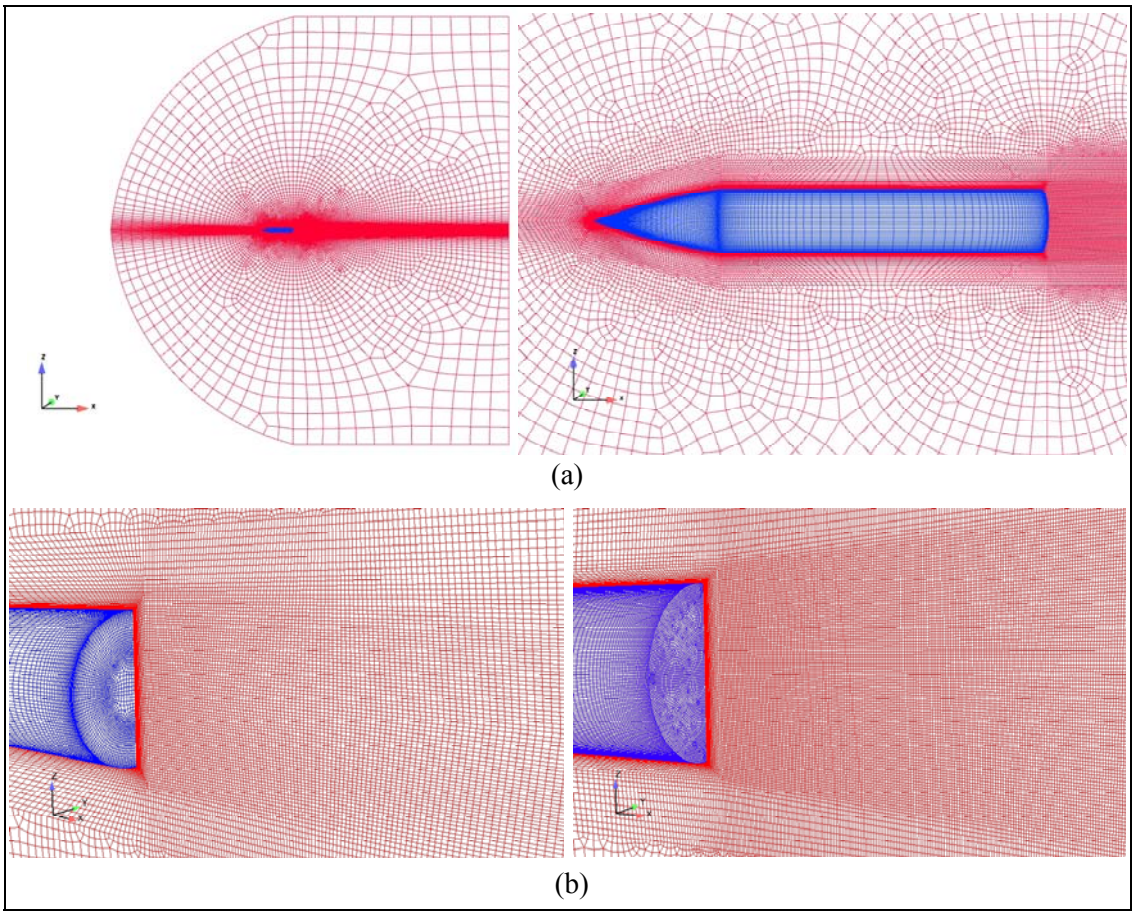

Figure 2. Computational mesh used for standard-base ANSR model: (a) RANS mesh (SB-1) and (b) close-up of the high-density mesh in the wake region of meshes SB-1 (left) and SB-2 (right).

the standard-base ANSR is shown in figure 2b. The surface mesh on the base of the ANSR was also made more uniform for the RANS/LES mesh. The mesh size increase was primarily due to the doubling of the circumferential mesh density, which was done to have nearly isotropic volume cells at the outer radial edge of the LES region of the mesh. As mentioned, the LES mesh in the wake only extended about 0.75 body lengths, then the mesh was stretched in the axial direction, as is normally done in RANS meshes. Therefore, the coherent structures present in the LES region will begin to be numerically dissipated by the RANS mesh upon leaving the LES zone.

The outer boundaries in the forward and radial directions were set as far-field (characteristics-based inflow/outflow), with standard temperature and pressure free-stream conditions (101.325 kPa, 288 K). The projectile wall was modeled as a no-slip, isothermal (288 K) wall boundary, rotating (clockwise when viewed from rear) around the x-axis at the specified spin rate. The projectile spin rates were determined from the muzzle exit twist, 10 cal./revolution (*13*), corresponding to a muzzle-exit nondimensional spin rate ($pd/2V$) of 0.315.

2.2 Navier-Stokes CFD

The commercially available CFD^{++} code (*17*), version 6.1.1, was used in this study. The CFD^{++} code can simulate a range of fluid dynamic phenomena, ranging from incompressible to hypersonic flow. The 3-D, time-dependent RANS equations are solved using the finite volume method. The implicit solver with dual time-stepping was used. The spatial discretization was a second-order, multidimensional total variation diminishing (TVD) polynomial interpolation scheme. Solutions to semi-infinite "Riemann problems" are used in CFD^{++} to provide upwind flux information to the underlying transport scheme. Approximate Riemann solvers are used to determine the higher-order fluxes to avoid spurious oscillations that may become physically unbounded if determined via fixed-stencil interpolation. Far-field absorbing layers were also used on the outer boundaries for the subsonic and transonic simulations.

The three-equation k-ε-R model, which solves transport equations for the turbulence kinetic energy, k, its dissipation rate, ε, and the undamped eddy viscosity, R, was used in the steady-state computations. This model provided the best performance across the Mach number range in ref 6. CFD^{++} also provides LES models and hybrid RANS/LES models, including the detached-eddy simulation (DES) model. The unsteady hybrid RANS/LES approach used the Batten-Goldberg model. The RANS/LES methodology of CFD^{++} is based on the solution of transport equations for the unresolved turbulence kinetic energy and its dissipation rate and incorporates anisotropy and low Reynolds number-damping effects in both LES and RANS modes. CFD^{++} reverts to a cubic k-ε model on RANS-type meshes and blends automatically to an anisotropic form of the Smagorinsky model in regions of uniformly refined mesh (*17*). Past unsteady RANS/LES simulations have been started from a steady-state solution using the k-ε-R model with good results (*6, 7*). However, the steady-state solutions used as the starting point for the unsteady RANS/LES simulations in this study were performed using the cubic k-ε turbulence model to provide the cleanest transition to the unsteady calculations. As a by-product, an additional set of steady-state CFD data is obtained for those Mach numbers at which the RANS/LES simulations were performed.

Most of the simulations were performed in parallel on an 1100-node, 4400-core Linux Networx Advanced Technology Cluster at the U.S. Army Research Laboratory DOD Supercomputing Resource Center. Each node has two dual-core, 3.0-GHz Intel Woodcrest processors. Some simulations were performed on an older 1024-node Linux Networx Evolocity II system with two 3.6-GHz Intel Xeon EM64T processors per node. The number of processors used for each steady-state run was such that about 145,000–150,000 cells were partitioned on each processor. The basic RANS calculations were run until steady state was achieved. The calculations took about 11–15 s of CPU time per iteration (wall-clock time was nearly the same) and convergence was achieved in about 600–800 iterations. The solution was deemed converged when the flow residuals had reduced at least 3 orders of magnitude and the aerodynamic coefficients changed less than about 0.5% over the last 100 iterations. The aerodynamic coefficients were the determining factor in convergence in all cases.

The double-precision solver with second-order spatial discretization was used. The maximum Courant-Friedrich-Lewy (CFL) number was chosen using the recommendations within the CFD^{++} solver; for the transonic flow regime ($0.7 < M < 1.4$), the CFL number is ramped from 1.0 to 75.0 over the first 100 iterations. The steady-state RANS calculations were performed at 14 Mach numbers over the range $0.6 \leq M \leq 2.5$ and at three angles of attack: $\alpha = 0°$, 2°, and 5°. The final solution of the appropriate steady-state case was used as the initial conditions for the unsteady RANS/LES calculations.

The unsteady RANS/LES calculations were performed at $\alpha = 2°$ and four Mach numbers: Mach 0.7, 0.8, 1.1, and 1.8. The time steps used were 4.0×10^{-6} s (Mach 0.7 and 0.8), 2.5×10^{-6} s (Mach 1.1), and 1.5×10^{-6} s (Mach 1.8). These values were determined based on having about 70 time steps within the period of the oscillations in the wake flow, assuming a Strouhal number of 0.25. Five inner iterations were performed at each time step. The number of processors used for the RANS/LES simulations was such that about 60,000 cells were partitioned on each processor. The unsteady calculations took about 6 s of CPU time per iteration, or about 30 s/time step, and were run for a total nondimensional time (based on Strouhal number) of 85–96 (Mach 0.7, 0.8, and 1.1) or 60 (Mach 1.8). The Mach 1.8 case had a shorter period of transition from the steady-state solution to the unsteady wake flow, so a shorter total time was used.

3. Results and Discussion

3.1 Grid Resolution Study

A grid resolution study was conducted for the Mach 0.7, 0.95, and 1.2 steady-state cases at $\alpha = 0°$, 2°, and 5°. The solutions for the coarse (SB-1a), medium (SB-1), and fine (SB-1b) meshes were compared for differences between the aerodynamic coefficients, and the results are shown in table 2. The table shows the percent differences in the aerodynamics coefficients between either the coarse (SB-1a) or fine (SB-1b) mesh and the medium mesh (SB-1). For $\alpha = 0°$, only the axial force and rolling moment are nonzero.

The percent differences in coefficients between the coarse and medium meshes are mostly less than 1%. The larger differences, still less than 5%, are mostly for the rolling moment and Magnus force and moments, which tend to be relatively small-valued coefficients. Nearly all the coefficients show a decrease in the percent difference between the medium and fine meshes compared to the difference between the medium and coarse meshes, as would be expected to show grid independence. Where there isn't a significant decrease, the relative change in the actual values is small. These results indicate that the coarse mesh was fairly well resolved. The medium mesh was designed based on past experience and knowledge of what type of mesh is

Table 2. Percent differences of aerodynamic coefficients from medium-sized mesh in grid resolution study.

Mach	Mesh	α	C_X (%)	C_Y (%)	C_N (%)	C_l (%)	C_m (%)	C_n (%)
0.7	Coarse–med	0	–0.68	—	—	0.20	—	—
		2	–0.89	–0.50	0.50	–0.92	1.66	–0.35
		5	–0.78	–3.02	0.40	–0.51	1.26	–4.29
	Med–fine	0	–0.67	—	—	–1.94	—	—
		2	–0.47	–0.75	0.52	–0.43	1.76	–1.10
		5	–0.35	–1.71	0.27	–0.28	0.86	–2.58
0.95	Coarse–med	0	–0.44	—	—	–2.24	—	—
		2	–0.21	–2.27	0.19	–0.69	0.99	–3.30
		5	–0.18	–1.20	0.15	–0.38	0.55	–1.39
	Med–fine	0	–0.14	—	—	–0.97	—	—
		2	–0.20	–1.88	0.85	–1.19	2.62	–2.84
		5	–0.12	–0.48	0.14	–0.48	0.30	–0.55
1.2	Coarse–med	0	–0.25	—	—	–0.67	—	—
		2	–0.47	–1.09	4.50	–0.47	19.25	–1.21
		5	–0.54	–0.53	0.18	–0.74	0.83	–0.42
	Med–fine	0	–0.09	—	—	0.74	—	—
		2	–0.11	0.92	–4.27	–0.22	–15.59	1.36
		5	0.02	–0.31	–0.34	–0.53	–1.34	–0.47

required to accurately predict the aerodynamic coefficients. These meshes tend to be of relatively high quality and high resolution. The coarsening of this mesh did not degrade the quality significantly, especially since the y^+ spacing was not modified. The Mach 1.2 normal-force and pitching-moment coefficients at $\alpha = 2°$ appear to be anomalous, giving 4.5% and 19.3%, respectively, between the coarse and medium meshes and –4.3% and –15.6%, respectively, between the medium and fine meshes. The actual values are such that those from the coarse and fine meshes are nearly equal. Therefore, the medium mesh, SB-1, was deemed appropriate for the steady-state computations, and all other meshes were based on it.

3.2 The 7-cal. ANSR Model Results

The aerodynamic data presented in this section is tabulated in appendix A. Figure 3 shows the drag coefficient as a function of Mach number, comparing the CFD predictions to the experimental data (*13, 14*). The CFD data is the drag at $\alpha = 2°$, while the experimental data is at the yaw angle in the flight range (0.4°–4.4°). The drag is approximately equal to the axial force coefficient at these low angles of attack. The experimental data is plotted for each of the three c.g. locations. CFD data is shown for the steady-state RANS simulations on both the RANS (SB-1) and RANS/LES (SB-2) meshes. Data is shown for unsteady RANS/LES simulations on the RANS mesh (SB-1) for two Mach numbers. The steady-state RANS simulations using the cubic k-ε model do slightly better than the k-ε-R model, which slightly overpredicts the drag over much of the Mach number range. The unsteady RANS/LES simulations vary, being closer to the k-ε-R steady predictions at Mach 0.7 and 1.1 and closer to the cubic k-ε steady predictions at Mach 0.8 and 1.8. The steady-state RANS predictions are adequate for drag prediction.

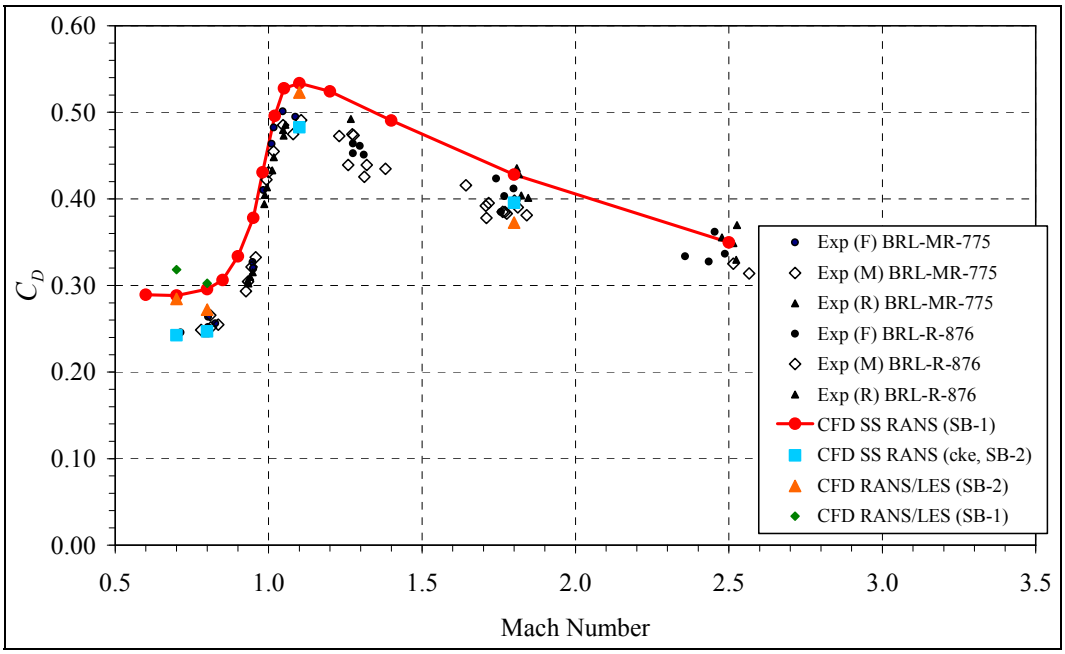

Figure 3. Drag coefficient (at $\alpha = 2°$) vs. Mach number: standard-base ANSR.

Figure 4 shows the roll-damping coefficient, which compares reasonably well with the experimental data. The roll-damping values were obtained at $\alpha = 2°$; however, C_{lp} was relatively insensitive to angle of attack up to the 5° investigated in this study. Over the Mach number range shown, the CFD values of C_{lp} are underpredicted (i.e., larger negative, so damping is overpredicted) by about 8%–15%. The trend of decreasing roll damping with Mach number is predicted very well by the CFD. The steady-state predictions with the cubic k-ε model and the unsteady RANS/LES predictions performed better than the steady-state calculations using the k-ε-R model. This is a similar result found for the M910 projectile (*7*). There is little difference between the RANS predictions using the cubic k-ε model and RANS/LES predictions, so the better prediction is solely due to the RANS region of the near-body grid. Even with these differences, the steady-state RANS simulations are adequate for C_{lp} predictions.

Figures 5 and 6 show the normal-force coefficient and pitching-moment coefficients at the three c.g. locations: forward (F), middle (M), and rear (R). Excellent agreement with the experimental data was found for all CFD predictions. There was very little difference between the steady-state RANS and unsteady RANS/LES predictions showing that the former computations are adequate for these coefficients. Figure 7 shows the normal force center of pressure, $x_{cp} = x_{cg} - \left(C_{m_\alpha} / C_{N_\alpha}\right)$, which is also predicted very well by all computational methods since it is based on C_{m_α} and C_{N_α}.

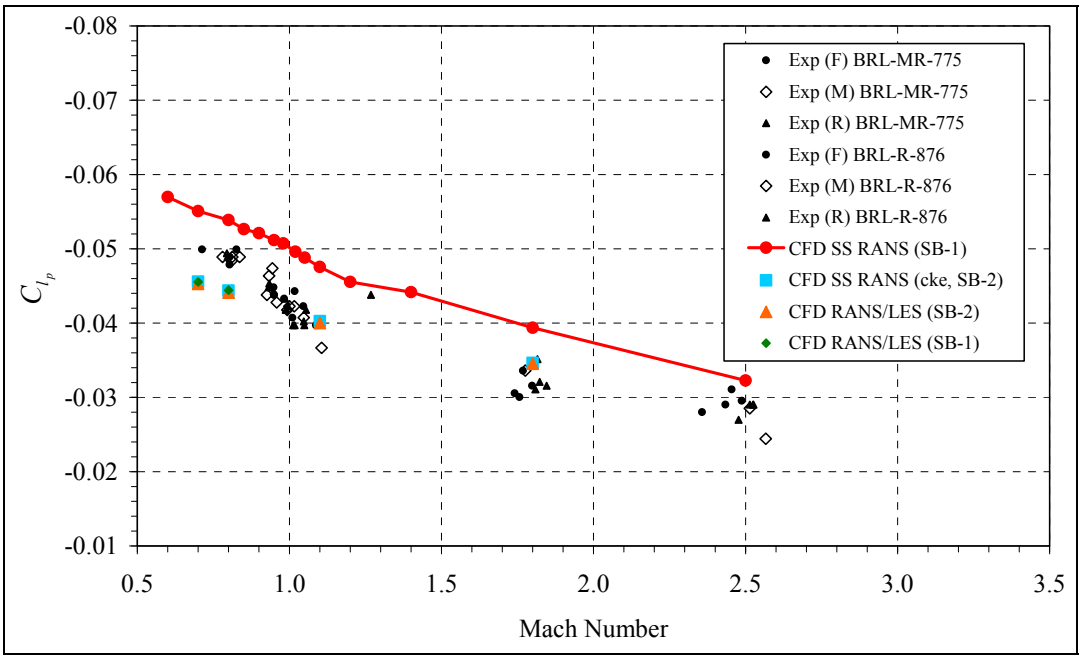

Figure 4. Roll-damping coefficient vs. Mach number: standard-base ANSR.

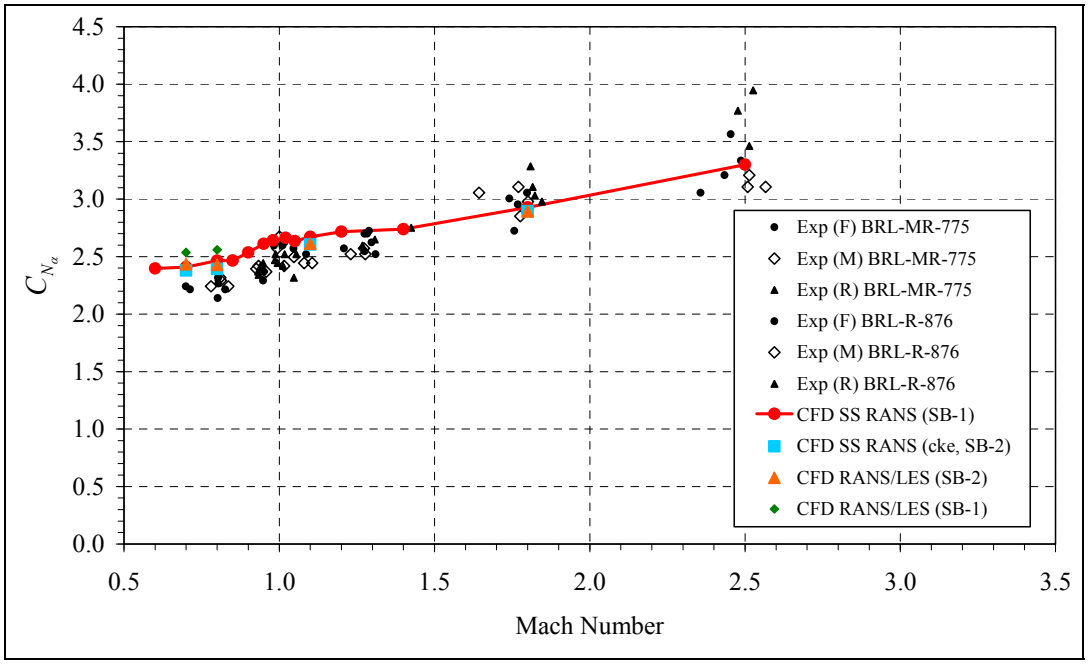

Figure 5. Normal force coefficient vs. Mach number: standard-base ANSR.

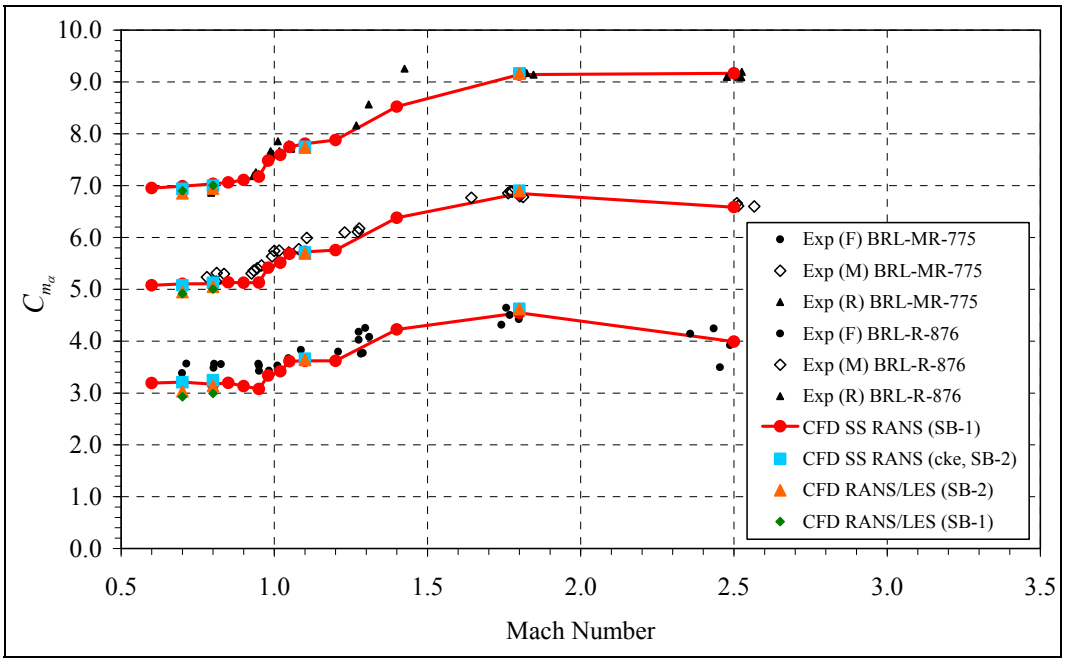

Figure 6. Pitching moment coefficient vs. Mach number: standard-base ANSR.

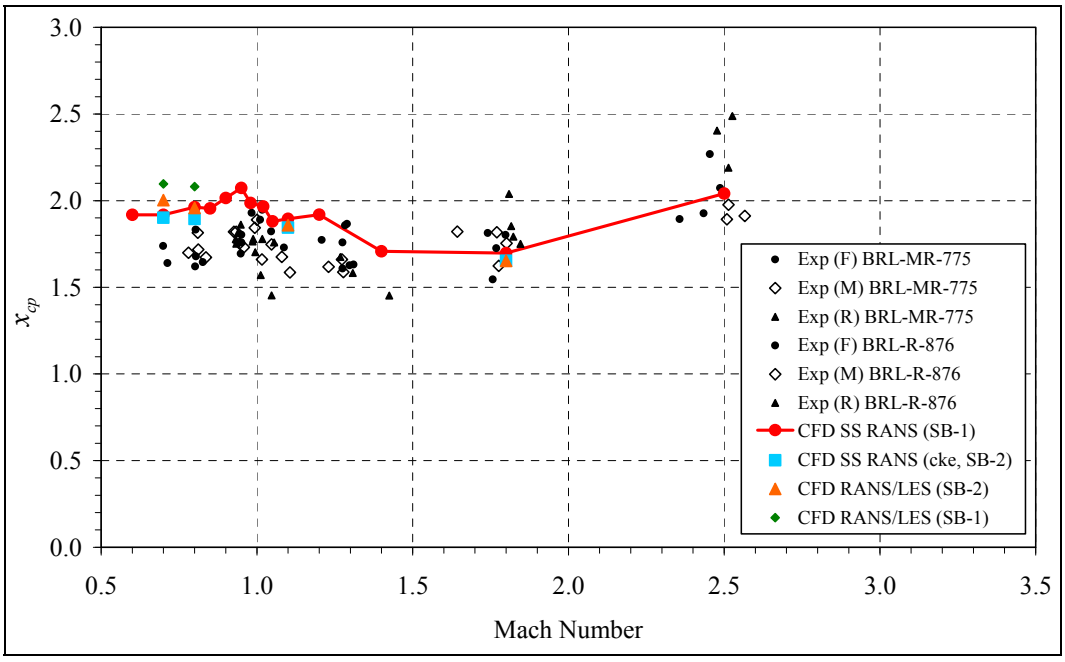

Figure 7. Normal force center-of-pressure location vs. Mach number: standard-base ANSR.

Figure 8 shows the pitch-damping coefficients at the three c.g. locations. The pitch-damping calculations were performed separate from the other calculations using a steady lunar coning motion described by Weinacht et al. (*18*). These are still steady-state computations but entail using a rotating reference frame to put the projectile body in a coning motion. The procedure

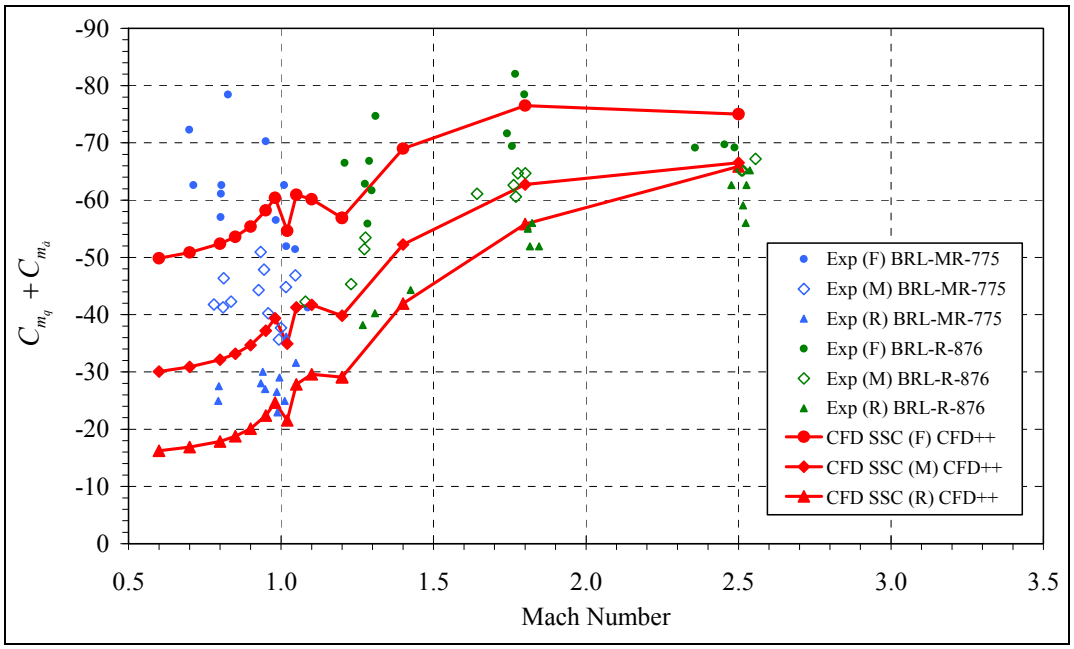

Figure 8. Pitch-damping moment coefficient vs. Mach number: standard-base ANSR.

was recently re-evaluated and more details can be found in DeSpirito et al. (*12*). (No unsteady RANS/LES computations were performed to obtain pitch damping.) The predicted pitch-damping values compare very well with the experimental data (*13, 14*), especially above the sonic velocity. The results at subsonic velocities show some degree of underprediction of the pitch damping, although there is significantly more scatter in the experimental data at these Mach numbers. Still, the CFD predictions fall within the error bounds, albeit at the ends of the error bounds at the lowest Mach numbers.

The primary goal of this report is to evaluate the prediction of the Magnus moment. Figure 9 shows the comparison of predicted and experimental Magnus moment for the three c.g. locations investigated. The predicted values fall within the data very well for $M \geq 1$. However, the experimental Magnus moment data shows a larger downward trend for $M < 1$ than the predicted values. Note there is an extremely large amount of scatter in the experimental data at all c.g. locations. Still, there is definitely a larger negative trend in the experimental data than there is in the CFD predictions. It is interesting to note that the steady-state RANS computations using the cubic k-ε model perform poorly at the lower Mach numbers. Therefore, this model was not chosen for the basic steady-state RANS computations in this and earlier studies (*6, 7*).

Time-accurate RANS/LES simulations do not improve the predictions, showing little change from the steady-state RANS predictions. This result differs from that found for the M910 projectile (*6, 7*), which showed an improvement in the Magnus moment prediction at the lower Mach numbers using unsteady RANS/LES computations. The ANSR does not exhibit the very large negative Magnus moment indicative of nonlinear effects, as did the M910. Weinacht (*4*) demonstrated that the shape of the projectile base (boattailed or not) is likely the dominant cause

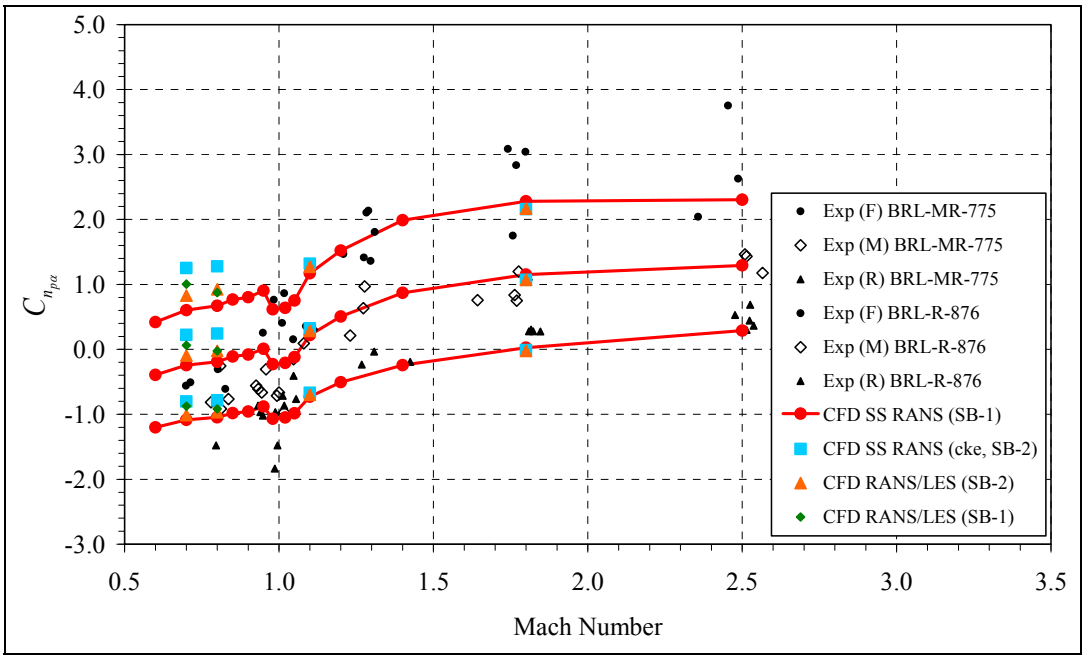

Figure 9. Magnus moment coefficient (at $\alpha = 2°$) vs. Mach number: standard-base ANSR.

of nonlinear Magnus moment. Weinacht showed that replacing a rounded base with a sharp corner nearly eliminated the nonlinear Magnus of a small-arms projectile. While there is definitely more scatter in the experimental data at Mach numbers <1, the variation of Magnus moment with angle of attack is still fairly linear (*13, 14*). It is reasonable that the nonlinear Magnus effects are captured better with the unsteady RANS/LES computations. Since there was not a large degree of nonlinearity in the ANSR Magnus moment, the steady-state computations performed adequately. However, the reason for the overpredicting of Magnus moment at the lower Mach numbers in this and other studies (*5–7, 12*) is unknown.

It is somewhat disturbing that the cubic k-ε model does not perform well since this is the model that the RANS/LES computations revert to in the RANS-mesh regions. Since this near-body RANS region is primarily responsible for the Magnus effects, one wonders if the cubic k-ε model is adversely affecting the unsteady RANS/LES predictions also.

Figure 10 shows a comparison of the Magnus moment of the standard-base and boattail ANSR. The experimental data for the boattail ANSR is from wind tunnel (WT) experiments (*15*), while the data for the standard-base ANSR is from free-flight, aeroballistic spark range experiments. The Magnus moment for the boattail ANSR is much higher than that for the standard-base ANSR at the lower Mach numbers. At the higher Mach numbers, the Magnus moment approaches that of the standard-base ANSR. The values of Magnus moment are again overpredicted; however, the peak just below Mach 1 is captured very well.

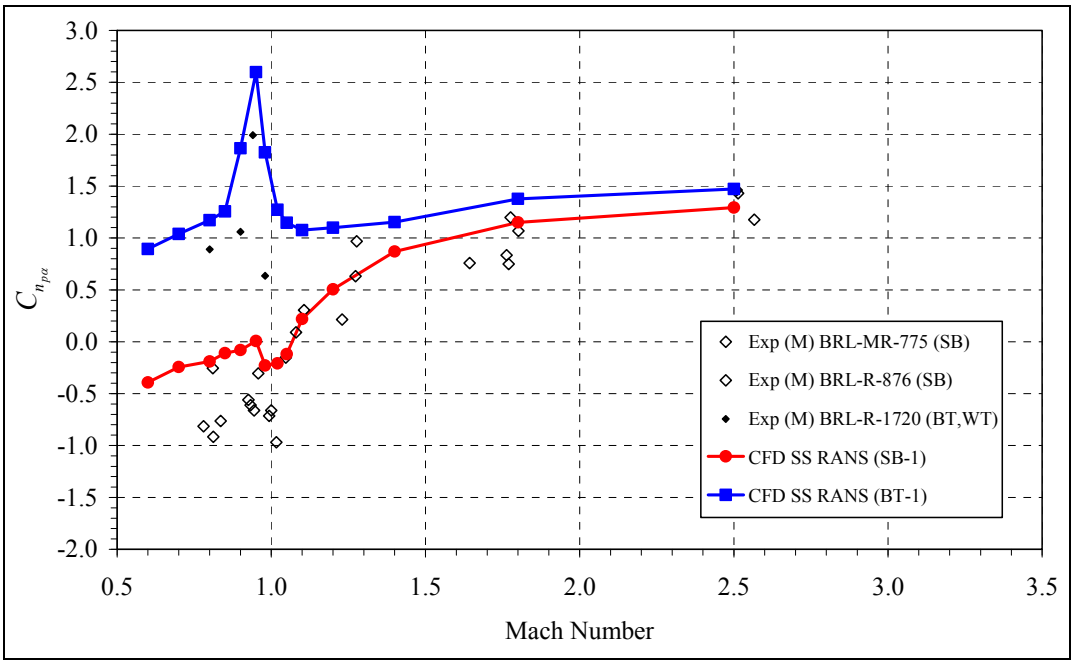

Figure 10. Magnus moment coefficient vs. Mach number: comparison of standard-base and boattail ANSR.

The flow field effects on Magnus force and moment are subtle and difficult to observe from flow field visualizations or plots of total forces or moments. A useful tool is to plot the distribution of the aerodynamic forces and moments along the projectile body to determine what part of the body contributes to each aerodynamic coefficient. The distribution of Magnus force and moment on the standard-base ANSR is shown in figure 11. The location of the c.g. is illustrated on the profile of the projectile (only results for the middle c.g. location are shown). The Magnus force is negative (normal pointing to the port side of the projectile) for a right-hand twist spin and positive angle of attack. There is very little difference in Magnus force and moment distributions between the steady-state RANS and unsteady RANS/LES computations. There is a reduction in the absolute value of Magnus force (figure 11a) over the last caliber of the ANSR body for the subsonic and transonic Mach numbers. This is likely due to an interaction of the wake flow on the asymmetric pressure distribution that generates the Magnus effect. There is a corresponding decrease in the value of the Magnus moment (figure 11b) over this same region.

The boattail ANSR (figure 12) also shows very little difference of the distribution of Magnus force and moment between the RANS and RANS/LES computations. There is a decrease in the total value of Magnus force (figure 12a) at all Mach numbers for the boattail ANSR compared to the standard-base ANSR. However, the shape of the distribution in the last caliber of the body is much different for the boattail configuration at the subsonic and transonic Mach numbers. The Magnus moment (figure 12b) shows similar trends.

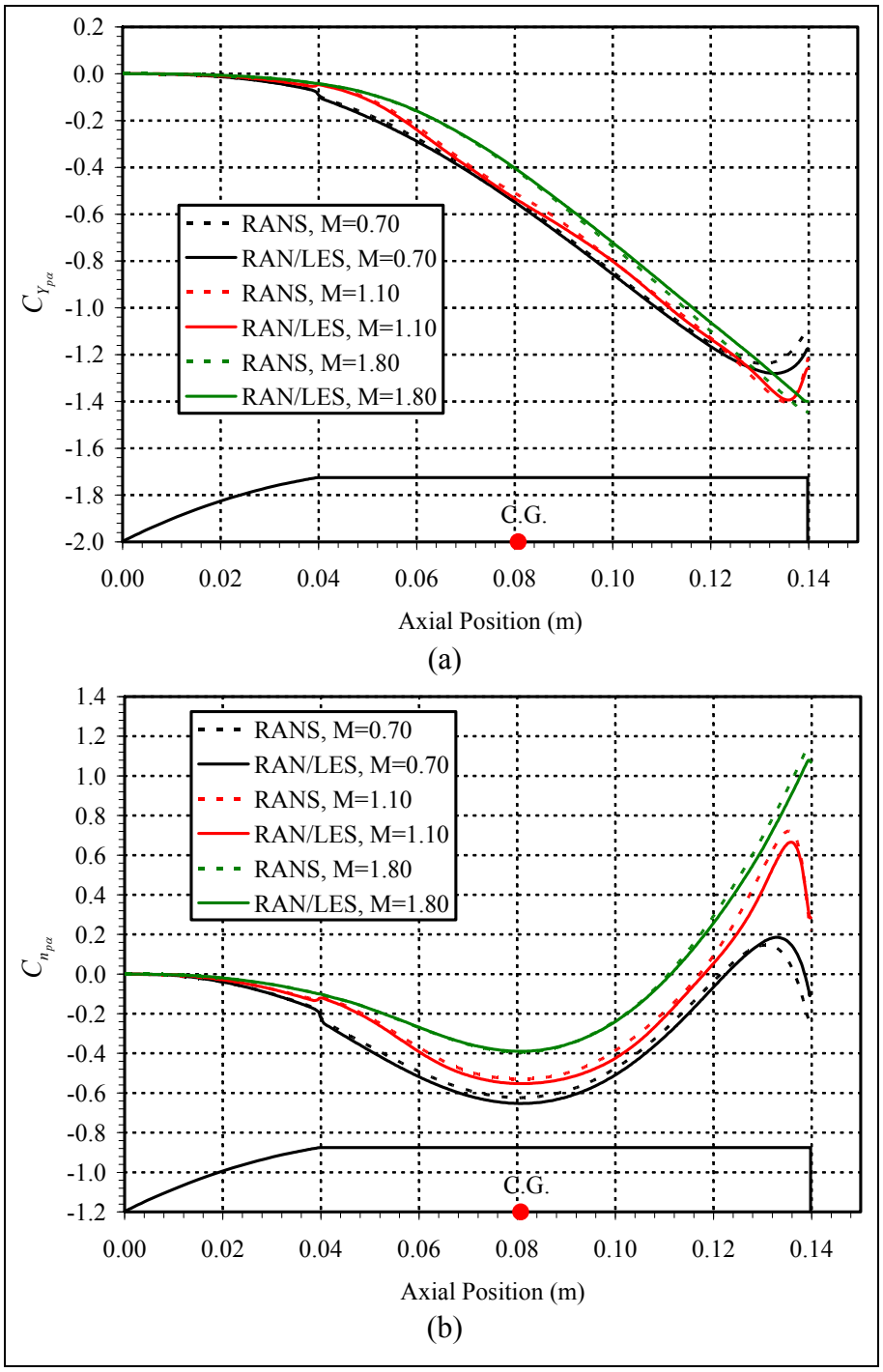

Figure 11. Distribution of Magnus (a) force and (b) moment coefficient (at $\alpha = 2°$) on standard-base ANSR: comparison of RANS and RANS/LES computations.

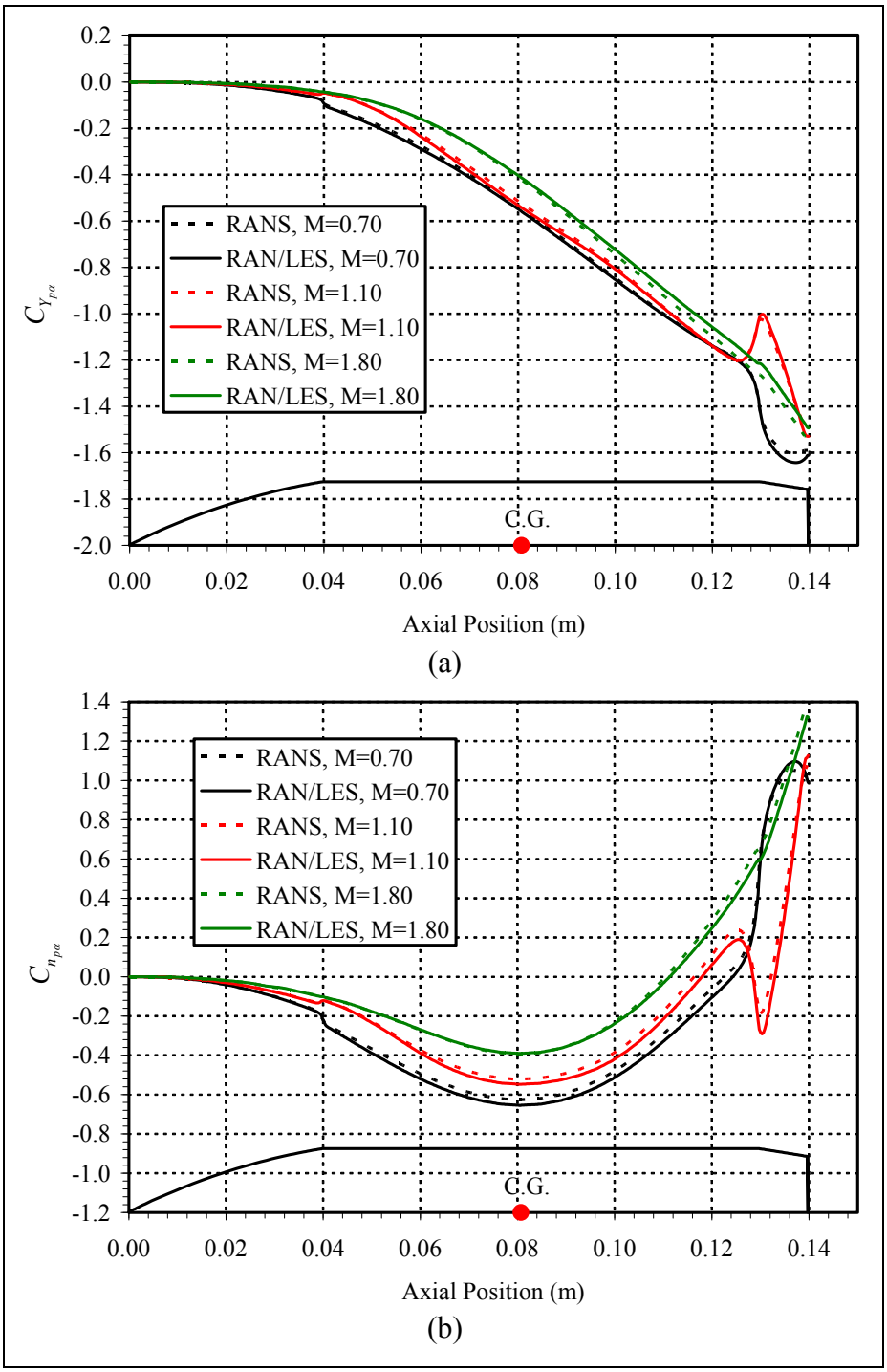

Figure 12. Distribution of Magnus (a) force and (b) moment coefficient (at $\alpha = 2°$) on boattail ANSR: comparison of RANS and RANS/LES computations.

Figure 13 shows the comparison of the distributions of Magnus force and moment computed from steady-state RANS computations for the standard-base and boattail version of the ANSR. There is little difference in the Magnus force and moment distributions for the supersonic Mach number. At subsonic and transonic Mach numbers, the Magnus force and moment distributions

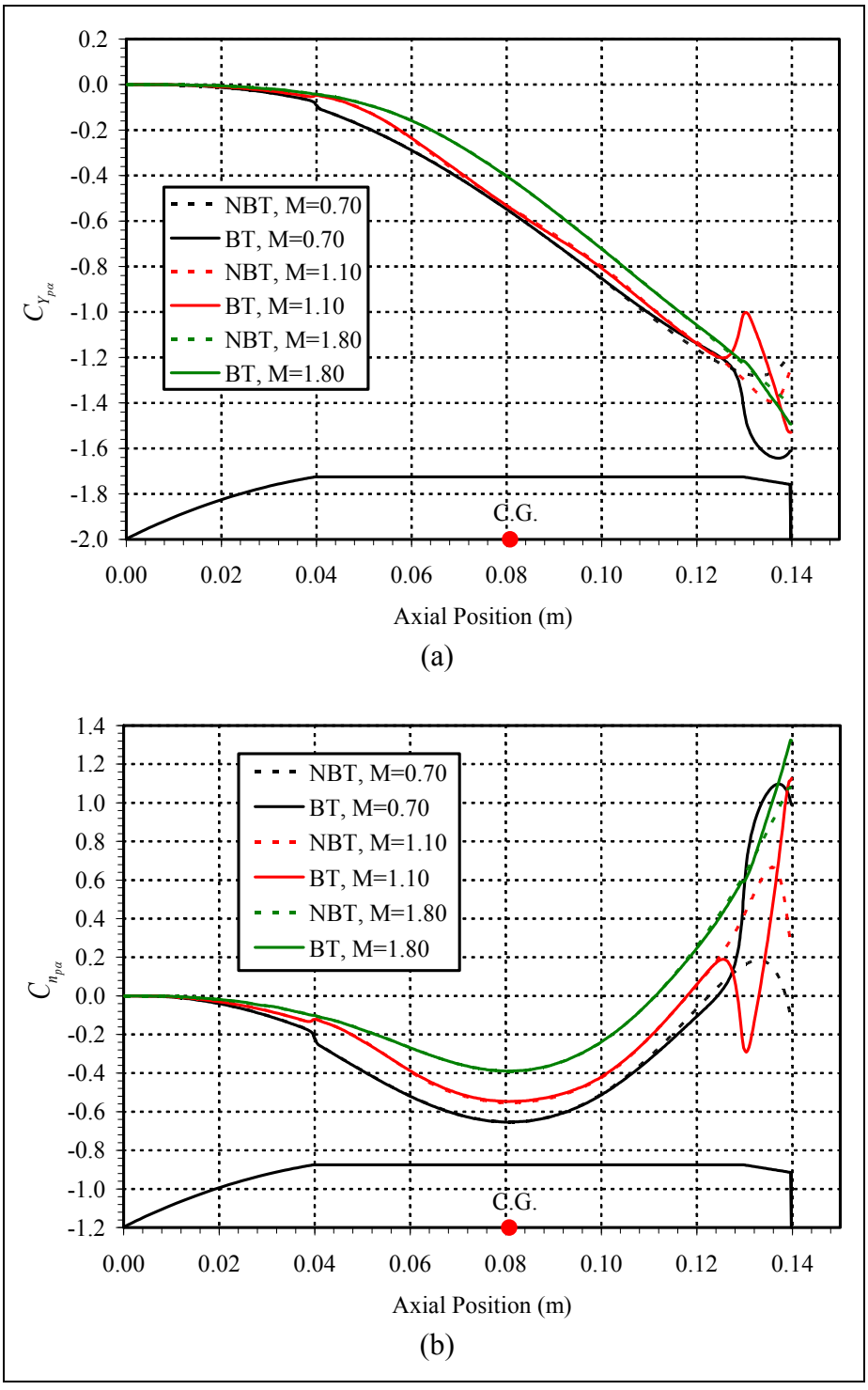

Figure 13. Distribution of Magnus (a) force and (b) moment coefficient (at $\alpha = 2°$): comparison of effect of ANSR base shape for steady-state RANS computations.

for the standard-base and boattail projectiles are nearly the same until the last caliber of the body. The data from figures 11–13 show that steady-state RANS computations predict the Magnus force and moment to the same level as unsteady RANS/LES computations for the ANSR configuration. Unsteady RANS/LES computations may very well be unnecessary for projectiles with sharp corners at the base, regardless if a boattail is present or not. Weinacht (*4*) found that the sharp-cornered base of the projectile nearly eliminated nonlinear Magnus effects. This may indicate that steady-state RANS simulations are adequate for projectiles that do not exhibit severe nonlinear Magnus moments.

Figure 14 shows typical instantaneous flow field patterns at $\alpha = 2°$ for the four Mach numbers at which the unsteady RANS/LES simulations were performed. Contours of Mach number are shown to illustrate the flow field for the standard-base and boattail ANSR configurations. The approximate extent of the LES mesh region is also shown on the images. As the coherent flow structures in the projectile wake leave the LES mesh region and enter the RANS (stretched) region of the mesh, they begin to rapidly dissipate due to numerical diffusion. The wake structures are also rotating about the x-axis due to the rotation of the projectile.

There are some small differences in the wake structure between the two base configurations, but they are generally the same. The differences are seen in figure 15, which shows contours of turbulent kinetic energy. The boattail directs the wake radially inward, generating a slightly smaller-diameter wake. As the Mach number increases to the supersonic regime, the unsteady wake begins to resemble that of a volume-average-type (steady-state RANS) flow field, which was illustrated previously (*6, 7*).

Figure 16 shows the comparison of the instantaneous flow field for the unsteady RANS/LES computations on the LES mesh (figure 16a) with that performed with the RANS mesh (figure 16b). Two boundaries are indicated in figure 16b; the first is where the nearly isotropic mesh extended. After this point, the mesh was stretched in the axial direction a small amount to the location of the vertical black line, where the mesh was then stretched at rates typical for RANS simulations. The near-wake flow field is very similar, and the RANS mesh did not produce overly poor results (e.g., see figure 9). Performing RANS/LES computations on RANS-like meshes is a suitable way to determine simulation parameters (e.g., time steps, inner iteration convergence, etc.) using less computational resources before moving onto the final computations on the LES mesh.

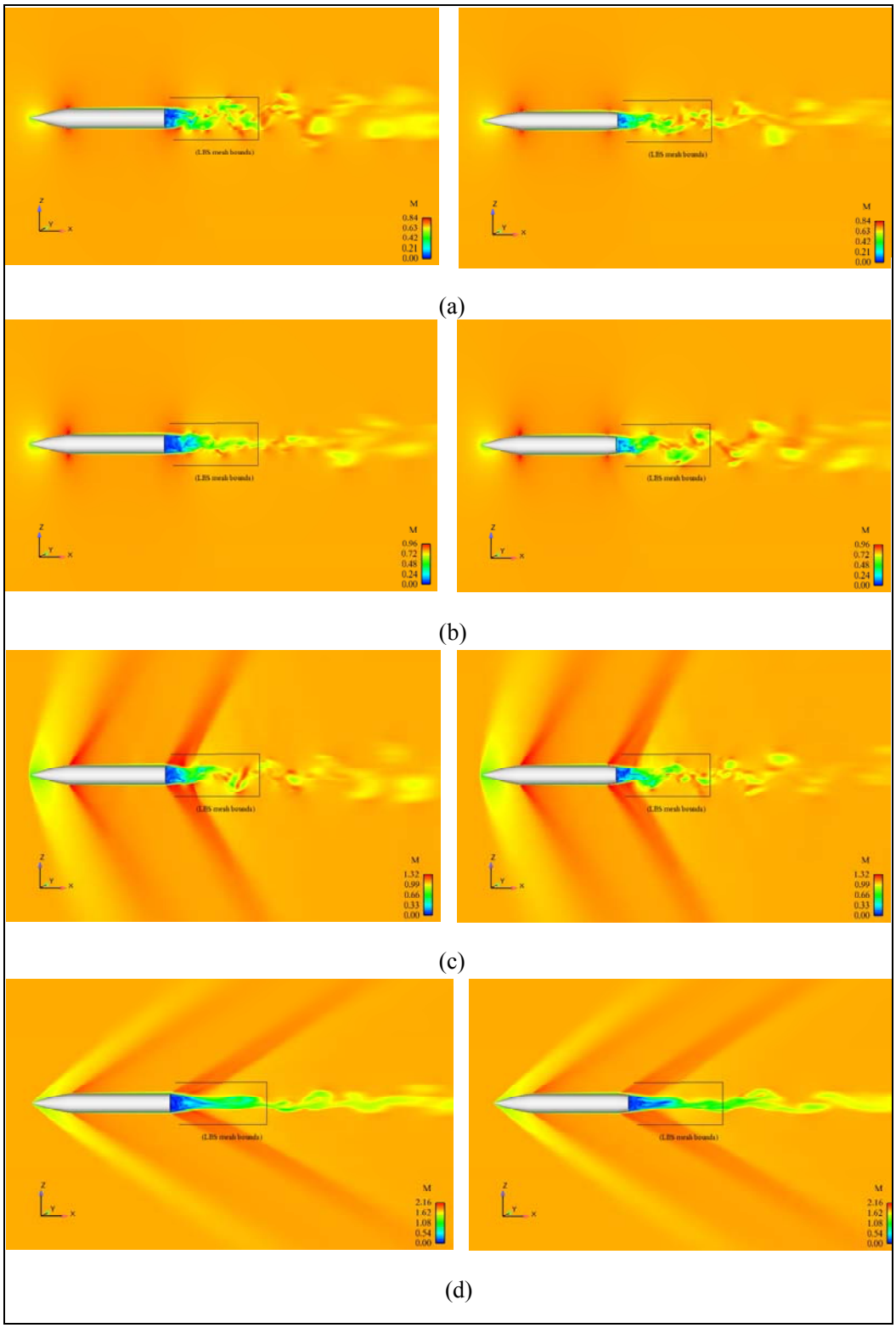

Figure 14. Instantaneous Mach number contours from unsteady RANS/LES calculations: standard-base and boattail ANSR at α = 2° and (a) Mach 0.7; (b) Mach 0.8; (c) Mach 1.1; and (d) Mach 1.8.

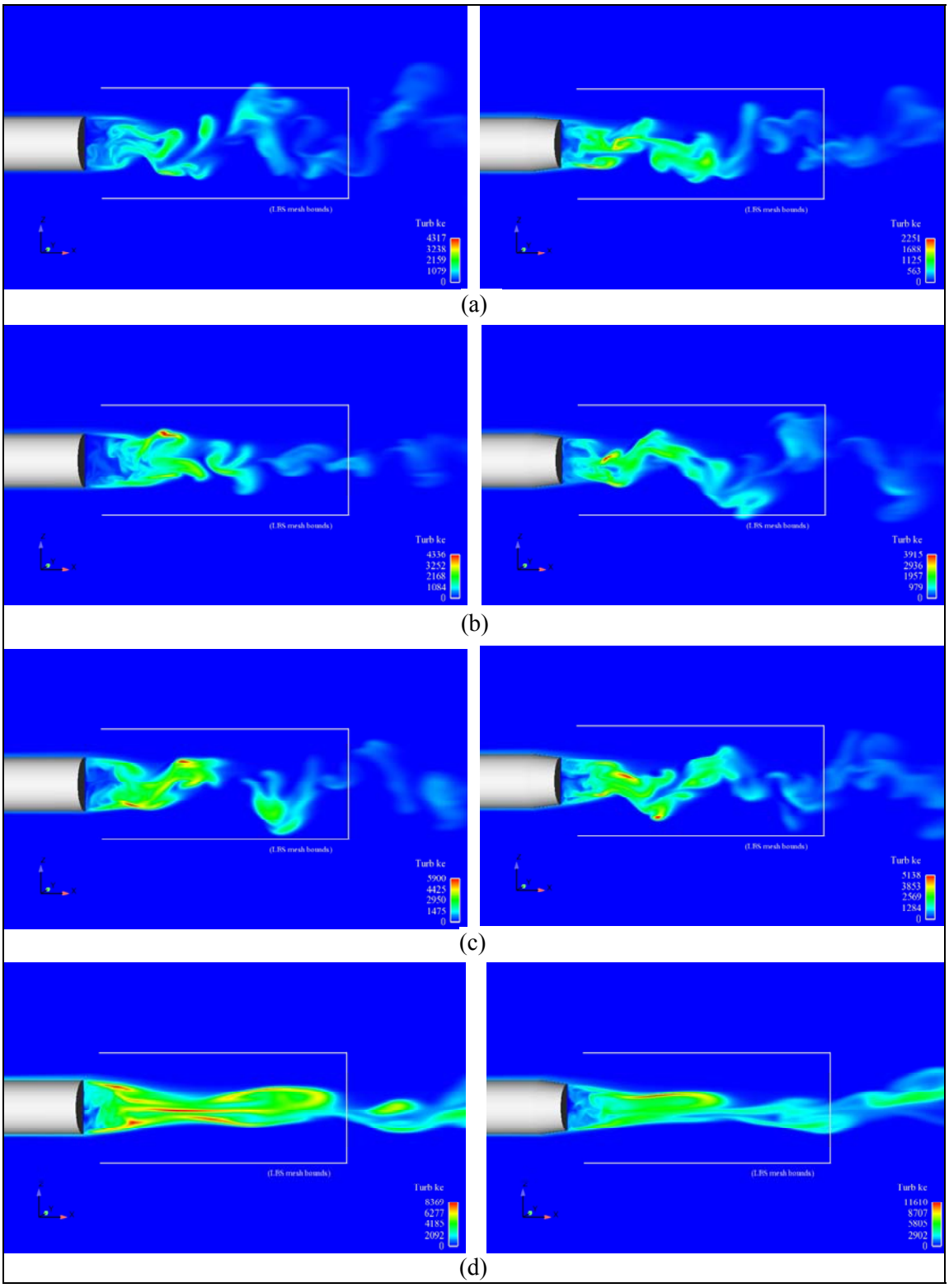

Figure 15. Instantaneous Mach number contours from unsteady RANS/LES calculations: standard-base and boattail ANSR at $\alpha = 2°$ and (a) Mach 0.7; (b) Mach 0.8; (c) Mach 1.1; and (d) Mach 1.8.

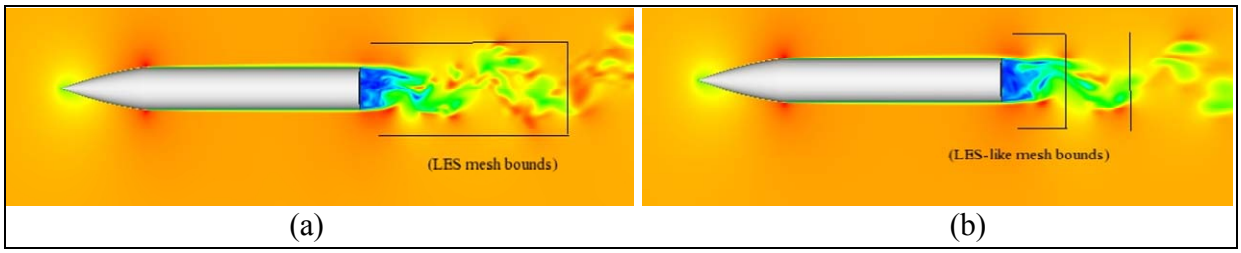

Figure 16. Instantaneous turbulent kinetic energy contours from unsteady RANS/LES calculations: standard-base ANSR at Mach 0.7 using (a) RANS/LES and (b) RANS mesh.

4. Summary and Conclusions

The aerodynamic coefficients of the 7-cal. U.S. Army-Navy Spinner Rocket were characterized using CFD calculations and validated using archival experimental data. The static aerodynamic coefficients, as well as the pitch-damping and roll-damping coefficients, were predicted well by the CFD. As expected, steady-state CFD calculations were adequate to predict these coefficients.

The prediction of Magnus moment was very good at Mach numbers >1. As found for other projectile configurations, the Magnus moment at Mach numbers <1 was overpredicted. However, unlike previous studies, unsteady hybrid RANS/LES calculations did not improve the prediction of Magnus moment at the lower Mach numbers. A highly nonlinear Magnus moment was not observed with the standard-base or boattailed ANSR projectiles. Both these designs have a sharp corner at the radial edge of the base, which has been shown (*4*) to reduce the nonlinear Magnus moment. It is possible that unsteady RANS/LES calculations may improve predictions for configurations where there is a highly nonlinear Magnus moment present. This will be the subject of further study.

Distributions of Magnus moment along the projectile body showed that the largest difference in Magnus moment between configurations and Mach numbers was in the last caliber of the body. Plotting these distributions is a very good way to determine the source of the contribution to each aerodynamic coefficient.

5. References

1. Sturek, W. B.; Schiff, L. B. Computations of the Magnus Effect for Slender Bodies in Supersonic Flow. *AIAA Journal* **1982**, *20* (12), 1724–1731.

2. Nietubicz, C. J.; Sturek, W. B.; Heavey, K. R. *Computations of Projectile Magnus Effect at Transonic Velocities*; BRL-TR-02515; U.S. Army Ballistics Research Laboratory: Aberdeen Proving Ground, MD, August 1983.

3. Sahu, J. *Transonic Navier-Stokes Computations for a Spinning Body of Revolution*; BRL-TR-3265; U.S. Army Ballistics Research Laboratory: Aberdeen Proving Ground, MD, September 1991.

4. Weinacht, P. Characterization of Small-Caliber Ammunition Performance Using a Virtual Wind Tunnel Approach; AIAA-2007-6579; *Proceedings of the AIAA Atmospheric Flight Mechanics Conference,* Hilton Head, SC, 20–23 August 2007.

5. Silton, S. I. *Navier-Stokes Computations for a Spinning Projectile From Subsonic to Supersonic Speeds*; ARL-TR-2850; U.S. Army Research Laboratory: Aberdeen Proving Ground, MD, September 2002.

6. DeSpirito, J.; Heavey, K. R. CFD Computation of Magnus Moment and Roll Damping Moment of a Spinning Projectile; AIAA-2004-4713; *Proceedings of the AIAA Atmospheric Flight Mechanics Conference,* Providence, RI, 16–19 August 2004.

7. DeSpirito, J.; Plostins, P. CFD Prediction of M910 Projectile Aerodynamics: Unsteady Wake Effect on Magnus Moment; AIAA-2007-6580; *Proceedings of the AIAA Atmospheric Flight Mechanics Conference,* Hilton Head, SC, 20–23 August 2007.

8. McCoy, R. L. *Modern Exterior Ballistics: The Launch and Flight Dynamics of Symmetric Projectiles*; Schiffer Books: Atglen, PA, 1998.

9. Simon, F.; Deck, S.; Guillen, P.; Sagaut, P. Reynolds-Averaged Navier-Stokes/Large-Eddy Simulations of Supersonic Base Flow. *AIAA Journal* **2006**, *44* (11), 2578–2590.

10. Simon, F.; Deck, S.; Guillen, P.; Cayzac, R.; Merlen, A. Zonal-Detached-Eddy Simulation of Projectiles in the Subsonic and Transonic Regimes. *AIAA Journal* **2007**, *45* (7), 1606–1619.

11. Simon, F.; Deck, S.; Guillen, P.; Cayzac, R.; Sagaut, P.; Merlen, A. RANS/LES Simulations of Projectiles With and Without Rotation in the Subsonic and Transonic Regimes. *Proceedings of the 23rd International Symposium on Ballistics*, Tarragona, Spain, April 2007.

12. DeSpirito, J.; Silton, S. I.; Weinacht, P. Navier-Stokes Predictions of Dynamic Stability Derivatives: Evaluation of Steady State Methods; AIAA-2008-0214; *Proceedings of the 46th Aerospace Sciences Meeting,* Reno, NV, 7–10 January 2008.

13. Schmidt, L. E.; Murphy, C. H. *The Aerodynamic Properties of the 7-Caliber Army-Navy Spinner Rocket in Transonic Flight*; BRL-MR-775; U.S. Army Ballistics Research Laboratory: Aberdeen Proving Ground, MD, March 1954.

14. Murphy, C. H.; Schmidt, L. E. *The Effect of Length on the Aerodynamic Characteristics of Bodies of Revolution in Supersonic Flight*; BRL-R-876; U.S. Army Ballistics Research Laboratory: Aberdeen Proving Ground, MD, August 1953.

15. Nielsen, G. I. T.; Platou, A. S. *The Effect of Conical Boattails on the Magnus Characteristics of Projectiles at Subsonic and Transonic Speeds*; BRL-R-1720; U.S. Army Ballistics Research Laboratory: Aberdeen Proving Ground, MD, June 1974.

16. Fluent, Inc. *Fluent 6.3 User's Guide*, Vol. 2; Lebanon, NH, 2006.

17. Metacomp Technologies, Inc. *CFD*$^{++}$ *User's Manual*; Agoura Hills, CA, 2006.

18. Weinacht, P.; Sturek, W. B.; Schiff, L. B. Navier-Stokes Predictions of Pitch Damping for Axisymmetric Projectiles. *AIAA J. Spacecraft & Rockets* **1997**, *34* (6), 753–761.

INTENTIONALLY LEFT BLANK.

Appendix. Aerodynamic Coefficient Data*

*Moment reference point is 4.036 cal. from nose in these tables.

Table A-1. Static aerodynamic coefficient data: standard-base configuration, 7-cal. ANSR.

Mach No.	α	C_X	C_{Xb}	C_{Xf}	C_Y	C_N	C_l	C_m	C_n	x_{cp}
0.60	0	0.2837	0.1815	0.1022	–0.0009	–0.0007	–0.0179	0.0020	0.0023	—
	2	0.2866	0.1853	0.1013	–0.0114	0.0837	–0.0179	0.1772	–0.0043	1.9183
	5	0.3000	0.2040	0.0960	–0.0379	0.2147	–0.0179	0.4344	0.0039	2.0132
0.70	0	0.2830	0.1838	0.0992	–0.0011	–0.0004	–0.0173	0.0011	0.0027	—
	2	0.2855	0.1873	0.0982	–0.0118	0.0841	–0.0174	0.1781	–0.0027	1.9180
	5	0.2986	0.2057	0.0929	–0.0381	0.2157	–0.0174	0.4376	0.0057	2.0076
0.80	0	0.2900	0.1892	0.1008	0.0000	–0.0002	–0.0167	0.0006	0.0000	—
	2	0.2929	0.1932	0.0997	–0.0120	0.0860	–0.0170	0.1782	–0.0021	1.9632
	5	0.3051	0.2111	0.0940	–0.0394	0.2194	–0.0168	0.4415	0.0094	2.0235
0.85	0	0.3007	0.1910	0.1097	0.0001	0.0000	–0.0163	0.0001	–0.0002	—
	2	0.3035	0.1949	0.1086	–0.0123	0.0861	–0.0166	0.1792	–0.0012	1.9545
	5	0.3155	0.2129	0.1026	–0.0392	0.2210	–0.0165	0.4413	0.0095	2.0388
0.90	0	0.3282	0.2009	0.1273	0.0003	–0.0001	–0.0162	0.0003	–0.0008	—
	2	0.3309	0.2046	0.1263	–0.0123	0.0885	–0.0164	0.1789	–0.0009	2.0149
	5	0.3426	0.2224	0.1201	–0.0400	0.2267	–0.0163	0.4419	0.0117	2.0870
0.95	0	0.3718	0.2167	0.1551	0.0000	0.0000	–0.0158	0.0001	0.0000	—
	2	0.3751	0.2212	0.1540	–0.0125	0.0912	–0.0161	0.1790	0.0001	2.0727
	5	0.3868	0.2388	0.1479	–0.0395	0.2325	–0.0159	0.4467	0.0118	2.1146
0.98	0	0.4251	0.2428	0.1823	0.0001	–0.0001	–0.0159	0.0001	–0.0002	—
	2	0.4278	0.2466	0.1811	–0.0118	0.0922	–0.0160	0.1890	–0.0025	1.9864
	5	0.4401	0.2648	0.1753	–0.0385	0.2363	–0.0157	0.4694	0.0076	2.0492
1.02	0	0.4911	0.2638	0.2272	0.0000	–0.0001	–0.0157	0.0003	0.0000	—
	2	0.4928	0.2666	0.2262	–0.0118	0.0930	–0.0156	0.1924	–0.0023	1.9665
	5	0.5060	0.2849	0.2212	–0.0386	0.2375	–0.0154	0.4790	0.0085	2.0188
1.05	0	0.5225	0.2689	0.2536	0.0000	0.0000	–0.0152	0.0000	–0.0001	—
	2	0.5249	0.2725	0.2523	–0.0122	0.0920	–0.0154	0.1983	–0.0013	1.8798
	5	0.5396	0.2923	0.2472	–0.0395	0.2366	–0.0152	0.4923	0.0111	1.9550
1.10	0	0.5272	0.2606	0.2666	0.0001	0.0000	–0.0150	0.0001	–0.0002	—
	2	0.5306	0.2645	0.2661	–0.0133	0.0932	–0.0150	0.1997	0.0024	1.8946
	5	0.5467	0.2844	0.2623	–0.0417	0.2380	–0.0149	0.4977	0.0189	1.9450
1.20	0	0.5181	0.2498	0.2683	0.0000	–0.0001	–0.0143	0.0003	0.0000	—
	2	0.5211	0.2535	0.2675	–0.0142	0.0949	–0.0143	0.2008	0.0056	1.9189
	5	0.5357	0.2720	0.2638	–0.0442	0.2363	–0.0143	0.5243	0.0271	1.8172
1.40	0	0.4817	0.2266	0.2551	0.0000	0.0000	–0.0135	0.0000	0.0000	—
	2	0.4875	0.2300	0.2575	–0.0156	0.0956	–0.0139	0.2226	0.0096	1.7073
	5	0.5029	0.2476	0.2553	–0.0479	0.2449	–0.0138	0.5615	0.0370	1.7429
1.80	0	0.4209	0.1848	0.2361	0.0000	0.0000	–0.0124	0.0000	0.0000	—
	2	0.4248	0.1888	0.2359	–0.0158	0.1022	–0.0124	0.2390	0.0126	1.6976
	5	0.4410	0.2061	0.2349	–0.0483	0.2705	–0.0123	0.5929	0.0458	1.8444
2.50	0	0.3426	0.1334	0.2092	0.0000	0.0000	–0.0102	0.0000	0.0000	—
	2	0.3460	0.1368	0.2093	–0.0141	0.1152	–0.0102	0.2298	0.0142	2.0409
	5	0.3603	0.1503	0.2100	–0.0421	0.3080	–0.0100	–0.6840	0.0478	2.2210

Table A-2. Aerodynamic derivative data: standard-base configuration, 7-cal. ANSR.

Mach No.	α	C_{N_α}	C_{m_α}	C_{l_p}	$C_{Y_{p\alpha}}$	$C_{n_{p\alpha}}$	$C_{m_q}+C_{m_{\dot\alpha}}$
0.60	0	—	—	–0.0567	—	—	–30.06
	2	2.3975	5.0772	–0.0570	–1.0337	–0.3926	
	5	2.4639	4.9839	–0.0570	–1.3790	0.1438	
0.70	0	—	—	–0.0549	—	—	–30.89
	2	2.4094	5.1031	–0.0551	–1.0768	–0.2438	
	5	2.4753	5.0208	–0.0551	–1.3868	0.2080	
0.80	0	—	—	–0.0530	—	—	–32.11
	2	2.4638	5.1069	–0.0539	–1.0952	–0.1892	
	5	2.5169	5.0653	–0.0535	–1.4360	0.3426	
0.85	0	—	—	–0.0519	—	—	–33.17
	2	2.4664	5.1339	–0.0526	–1.1157	-0.1093	
	5	2.5352	5.0635	–0.0525	–1.4288	0.3447	
0.90	0	—	—	–0.0515	—	—	–34.70
	2	2.5362	5.1260	–0.0521	–1.1231	–0.0800	
	5	2.6014	5.0701	–0.0516	–1.4563	0.4269	
0.95	0	—	—	–0.0502	—	—	–37.19
	2	2.6123	5.1286	–0.0512	–1.1377	0.0083	
	5	2.6677	5.1257	–0.0506	–1.4378	0.4314	
0.98	0	—	—	–0.0504	—	—	–39.38
	2	2.6421	5.4152	–0.0507	–1.0725	–0.2288	
	5	2.7110	5.3863	–0.0499	–1.4034	0.2769	
1.02	0	—	—	–0.0498	—	—	–34.92
	2	2.6634	5.5120	–0.0496	–1.0771	-0.2081	
	5	2.7247	5.4964	–0.0488	–1.4054	0.3100	
1.05	0	—	—	–0.0482	—	—	–41.26
	2	2.6355	5.6827	–0.0488	–1.1072	-0.1185	
	5	2.7143	5.6483	–0.0481	–1.4378	0.4054	
1.10	0	—	—	–0.0477	—	—	–41.73
	2	2.6717	5.7213	–0.0475	–1.2120	0.2194	
	5	2.7311	5.7107	–0.0473	–1.5204	0.6897	
1.20	0	—	—	–0.0453	—	—	–39.80
	2	2.7180	5.7544	–0.0455	–1.2945	0.5053	
	5	2.7114	6.0159	–0.0454	–1.6106	0.9863	
1.40	0	—	—	–0.0428	—	—	–52.25
	2	2.7394	6.3794	–0.0442	–1.4233	0.8701	
	5	2.8093	6.4420	–0.0438	–1.7437	1.3464	
1.80	0	—	—	–0.0395	—	—	–62.74
	2	2.9289	6.8489	–0.0394	–1.4381	1.1502	
	5	3.1038	6.8023	–0.0390	–1.7585	1.6674	
2.50	0	—	—	–0.0323	—	—	–66.54
	2	3.3004	6.5845	–0.0323	–1.2867	1.2931	
	5	3.5335	6.4132	–0.0319	–1.5347	1.7403	

Table A-3. Static aerodynamic coefficient data: boattail configuration, 7-cal. ANSR.

Mach No.	α	C_X	C_{Xb}	C_{Xf}	C_Y	C_N	C_l	C_m	C_n	x_{cp}
0.60	0	0.1981	0.0686	0.1295	–0.0005	0.0008	–0.0155	–0.0019	0.0014	—
	2	0.2018	0.0724	0.1294	–0.0171	0.0672	–0.0159	0.2167	0.0098	0.8109
	5	0.2150	0.0884	0.1266	–0.0498	0.1775	–0.0158	0.5240	0.0334	1.0831
0.70	0	0.1940	0.0654	0.1286	0.0004	0.0004	–0.0152	–0.0010	–0.0009	—
	2	0.1976	0.0692	0.1284	–0.0175	0.0674	–0.0154	0.2191	0.0114	0.7869
	5	0.2104	0.0849	0.1255	–0.0501	0.1767	–0.0153	0.5340	0.0357	1.0133
0.80	0	0.1938	0.0610	0.1328	0.0000	0.0002	–0.0147	–0.0004	0.0001	—
	2	0.1971	0.0646	0.1325	–0.0179	0.0671	–0.0150	0.2247	0.0129	0.6877
	5	0.2094	0.0800	0.1294	–0.0513	0.1758	–0.0148	0.5494	0.0396	0.9106
0.85	0	0.2028	0.0576	0.1452	0.0001	0.0007	–0.0144	–0.0018	–0.0002	—
	2	0.2062	0.0610	0.1452	–0.0181	0.0665	–0.0147	0.2304	0.0138	0.5703
	5	0.2187	0.0756	0.1431	–0.0524	0.1749	–0.0146	0.5620	0.0435	0.8236
0.90	0	0.2275	0.0492	0.1784	0.0000	0.0002	–0.0142	–0.0006	0.0000	—
	2	0.2302	0.0519	0.1783	–0.0203	0.0637	–0.0144	0.2448	0.0205	0.1946
	5	0.2399	0.0637	0.1762	–0.0574	0.1680	–0.0143	0.5991	0.0586	0.4691
0.95	0	0.2818	0.0413	0.2405	0.0000	0.0000	–0.0140	0.0000	–0.0001	—
	2	0.2852	0.0450	0.2402	–0.0222	0.0722	–0.0142	0.2369	0.0286	0.7556
	5	0.3002	0.0631	0.2372	–0.0600	0.1945	–0.0141	0.5652	0.0720	1.1302
0.98	0	0.3463	0.0833	0.2630	0.0000	–0.0001	–0.0139	0.0002	0.0000	—
	2	0.3495	0.0870	0.2626	–0.0192	0.0791	–0.0142	0.2290	0.0201	1.1398
	5	0.3646	0.1054	0.2592	–0.0532	0.2082	–0.0140	0.5554	0.0529	1.3679
1.02	0	0.4374	0.1347	0.3028	0.0000	0.0000	–0.0136	0.0000	0.0000	—
	2	0.4410	0.1388	0.3022	–0.0171	0.0833	–0.0139	0.2230	0.0140	1.3585
	5	0.4584	0.1597	0.2987	–0.0493	0.2166	–0.0138	0.5461	0.0415	1.5145
1.05	0	0.4555	0.1372	0.3184	0.0000	0.0000	–0.0135	0.0000	0.0000	—
	2	0.4602	0.1417	0.3185	–0.0166	0.0834	–0.0137	0.2218	0.0126	1.3784
	5	0.4778	0.1626	0.3152	–0.0479	0.2180	–0.0136	0.5432	0.0381	1.5442
1.10	0	0.4736	0.1414	0.3322	0.0000	0.0000	–0.0133	0.0000	0.0000	—
	2	0.4784	0.1460	0.3324	–0.0163	0.0849	–0.0133	0.2220	0.0118	1.4206
	5	0.4961	0.1669	0.3292	–0.0472	0.2203	–0.0134	0.5458	0.0364	1.5582
1.20	0	0.4649	0.1426	0.3223	–0.0001	0.0000	–0.0129	0.0000	0.0001	—
	2	0.4692	0.1468	0.3223	–0.0164	0.0853	–0.0129	0.2289	0.0121	1.3529
	5	0.4878	0.1678	0.3200	–0.0481	0.2242	–0.0129	0.5612	0.0388	1.5332
1.40	0	0.4360	0.1400	0.2960	0.0000	0.0001	–0.0123	–0.0001	0.0001	—
	2	0.4420	0.1439	0.2981	–0.0167	0.0902	–0.0126	0.2375	0.0127	1.4010
	5	0.4604	0.1629	0.2975	–0.0503	0.2355	–0.0126	0.5886	0.0438	1.5365
1.80	0	0.3872	0.1236	0.2636	0.0000	0.0000	–0.0114	0.0000	0.0000	—
	2	0.3908	0.1270	0.2639	–0.0168	0.1029	–0.0114	0.2379	0.0151	1.7240
	5	0.4071	0.1432	0.2640	–0.0501	0.2599	–0.0113	0.6205	0.0503	1.6486
2.50	0	0.3217	0.0953	0.2264	0.0000	0.0000	–0.0095	0.0000	–0.0001	—
	2	0.3256	0.0984	0.2272	–0.0150	0.1120	–0.0096	0.2383	0.0162	1.9086
	5	0.3399	0.1111	0.2288	–0.0430	0.3005	–0.0094	0.5790	0.0498	2.1094

Table A-4. Aerodynamic derivative data: boattail configuration, 7-cal. ANSR.

Mach No.	α	C_{N_α}	C_{m_α}	C_{l_p}	$C_{Y_{p\alpha}}$	$C_{n_{p\alpha}}$
0.60	0	—	—	–0.0494	—	—
	2	1.9257	6.2107	–0.0506	–1.5561	0.8947
	5	2.0362	6.0128	–0.0503	–1.8153	1.2168
0.70	0	—	—	–0.0481	—	—
	2	1.9318	6.2767	–0.0490	–1.5891	1.0389
	5	2.0268	6.1265	–0.0486	–1.8264	1.3021
0.80	0	—	—	–0.0468	—	—
	2	1.9227	6.4379	–0.0475	–1.6252	1.1707
	5	2.0168	6.3032	–0.0471	–1.8680	1.4424
0.85	0	—	—	–0.0458	—	—
	2	1.9048	6.6015	–0.0467	–1.6440	1.2571
	5	2.0073	6.4482	–0.0463	–1.9101	1.5829
0.90	0	—	—	–0.0450	—	—
	2	1.8262	7.0153	–0.0457	–1.8447	1.8650
	5	1.9270	6.8735	–0.0454	–2.0898	2.1342
0.95	0	—	—	–0.0445	—	—
	2	2.0689	6.7869	–0.0452	–2.0232	2.5990
	5	2.2317	6.4848	–0.0447	–2.1862	2.6235
0.98	0	—	—	–0.0442	—	—
	2	2.2660	6.5626	–0.0450	–1.7494	1.8252
	5	2.3884	6.3727	–0.0444	–1.9393	1.9255
1.02	0	—	—	–0.0431	—	—
	2	2.3869	6.3909	–0.0441	–1.5576	1.2705
	5	2.4847	6.2653	–0.0437	–1.7970	1.5128
1.05	0	—	—	–0.0427	—	—
	2	2.3911	6.3545	–0.0436	–1.5116	1.1472
	5	2.5010	6.2320	–0.0431	–1.7454	1.3868
1.10	0	—	—	–0.0421	—	—
	2	2.4323	6.3614	–0.0423	–1.4829	1.0766
	5	2.5276	6.2628	–0.0425	–1.7188	1.3267
1.20	0	—	—	–0.0409	—	—
	2	2.4445	6.5588	–0.0409	–1.4911	1.0988
	5	2.5730	6.4395	–0.0410	–1.7515	1.4126
1.40	0	—	—	–0.0390	—	—
	2	2.5831	6.8066	–0.0400	–1.5211	1.1521
	5	2.7021	6.7539	–0.0400	–1.8326	1.5951
1.80	0	—	—	–0.0363	—	—
	2	2.9489	6.8177	–0.0362	–1.5254	1.3773
	5	2.9819	7.1189	–0.0360	–1.8263	1.8322
2.50	0	—	—	–0.0301	—	—
	2	3.2099	6.8287	–0.0304	–1.3610	1.4719
	5	3.4481	6.6433	–0.0300	–1.5663	1.8129

INTENTIONALLY LEFT BLANK.

List of Symbols, Abbreviations, and Acronyms

ANSR	Army-Navy Spinner Rocket
C_D	drag coefficient
CFD	computational fluid dynamic
CFL	Courant-Friedrich-Lewy
c.g.	center of gravity
C_l	roll moment coefficient
C_{l_p}	roll-damping coefficient
C_m	pitching moment coefficient
C_{m_α}	slope of pitching moment coefficient with angle of attack
$C_{m_q} + C_{m_{\dot{\alpha}}}$	pitch-damping moment coefficient sum
C_N	normal force coefficient
C_{N_α}	slope of normal force coefficient with angle of attack
C_n	side moment coefficient
$C_{n_{p\alpha}}$	Magnus moment coefficient
C_p	pressure coefficient
C_X	total axial force coefficient
C_{Xb}	axial force coefficient on projectile base
C_{Xf}	axial force coefficient on projectile forebody
C_Y	side force coefficient
$C_{Y_{p\alpha}}$	Magnus force coefficient
d	missile base diameter, m
DES	detached-eddy simulation
k	turbulence kinetic energy, m^2/s^2
LES	large-eddy simulation
M	Mach number

p	pressure, N/m^2; projectile spin rate, radians/s
q_∞	dynamic pressure, ½ ρV^2, N/m^2
R	undamped eddy viscosity, m^2/s
RANS	Reynolds-averaged Navier-Stokes
S	projectile cross-sectional area, m^2
3-D	three dimensional
TVD	total variation diminishing
V	free stream velocity, m/s
WT	wind tunnel
x, y, z	axial, horizontal, and vertical body axes
x_{cg}	center of gravity location
x_{cp}	normal force center of pressure location, $x_{cp} = x_{cg} - \left(C_{m_\alpha} / C_{N_\alpha}\right)$, cal.
α	angle of attack
ε	turbulence dissipation rate, m^2/s^3
ρ	density, kg/m^3

NO. OF
COPIES ORGANIZATION

1 (PDF only) DEFENSE TECHNICAL INFORMATION CTR
DTIC OCA
8725 JOHN J KINGMAN RD
STE 0944
FORT BELVOIR VA 22060-6218

1 DIRECTOR
US ARMY RESEARCH LAB
IMNE ALC HRR
2800 POWDER MILL RD
ADELPHI MD 20783-1197

1 DIRECTOR
US ARMY RESEARCH LAB
RDRL CIM L
2800 POWDER MILL RD
ADELPHI MD 20783-1197

1 DIRECTOR
US ARMY RESEARCH LAB
RDRL CIM P
2800 POWDER MILL RD
ADELPHI MD 20783-1197

ABERDEEN PROVING GROUND

1 DIR USARL
RDRL CIM G (BLDG 4600)

NO. OF COPIES	ORGANIZATION
1	AIR FORCE RESEARCH LABORATORY AFRL MNAV G ABATE 101 W EGLIN BLVD STE 333 EGLIN AFB FL 32542-6810
3	US ARMY AMRDEC AMSAM RD SS AT R W KRETZSHMAR L AUMAN E VAUGHN REDSTONE ARSENAL AL 35898-5000
1	PM TMAS SFAE ASM TMAMS R KOWALSKI BLDG 171A PICATINNY ARSENAL NJ 07806-5000
1	COMMANDER US ARMY TACOM ARDEC AMSRD AAR AEM C P MAGNOTTI BLDG 61S PICATINNY ARSENAL NJ 07806-5000
1	COMMANDER US ARMY ARDEC ASMRD AAR AEP E C KESSLER BLDG 3022 PICATINNY ARSENAL NJ 07806-5000
1	COMMANDER US ARMY ARDEC ASMRD AAR AEP E C STOUT BLDG 94 PICATINNY ARSENAL NJ 07806-5000
2	COMMANDER US ARMY ARDEC AMSRD AAR AEM A S CHUNG M DUCA BLDG 94 PICATINNY ARSENAL NJ 07806-5000

NO. OF COPIES	ORGANIZATION
1	COMMANDER US ARMY ARDEC AMSRD AAR AEM A A FARINA BLDG 65N PICATINNY ARSENAL NJ 07806-5000
10	COMMANDER US ARMY ARDEC AMSRD AAR AEM A J GRAU S HAN W KOENIG C LIVECCHIA G MALEJKO T RECCHIA W TOLEDO R TROHANOWSKY E VAZQUEZ C WILSON BLDG 95 PICATINNY ARSENAL NJ 07806-5000
1	COMMANDER US ARMY ARDEC AMSRD AAR AEM A B WONG BLDG 61S PICATINNY ARSENAL NJ 07806-5000
1	COMMANDER US ARMY ARDEC AMSRD AAR AEM A L YEE BLDG 19 PICATINNY ARSENAL NJ 07806-5000
1	US ARMY TACOM ARDEC CCAC AMSTA AR CCL C G FLEMING BLDG 65N PICATINNY ARSENAL NJ 07806-5000
1	US ARMY TACOM ARDEC CCAC AMSTA AR CCL B J MIDDLETON BLDG 65N PICATINNY ARSENAL NJ 07806-5000

NO. OF COPIES ORGANIZATION

1 US ARMY TACOM ARDEC
ASIC PRGM INTEGRATION OFC
J A RESCH
BLDG 1
PICATINNY ARSENAL NJ 07801

1 US ARMY TACOM ARDEC
AMSRD AAR AEW M(D)
M D MINISI
BLDG 65N
PICATINNY ARSENAL NJ 07806-5000

1 US ARMY TACOM ARDEC
AMSRD AR CCL C
S SPICKERT-FULTON
BLDG 65N
PICATINNY ARSENAL NJ 07806-5000

1 US ARMY TACOM ARDEC
AMSRD AAR AEM T
M NICOLICH
BLDG 65S
PICATINNY ARSENAL NJ 07806-5000

1 US ARMY TACOM ARDEC
AMSRD AAR AEM S
S MUSALLI
BLDG 65S
PICATINNY ARSENAL NJ 07806-5000

1 US ARMY TACOM ARDEC
AMSRD AAR AEM I
R MAZESKI
BLDG 61N
PICATINNY ARSENAL NJ 07806-5000

1 US ARMY ARDEC
AMSRD AAR AEM M
V GONSALVES
BLDG 61S
PICATINNY ARSENAL NJ 07806-5000

1 US ARMY ARDEC
AMSRD AAR AEM S
D DIEDALIS
BLDG 162N
PICATINNY ARSENAL NJ 07806-5000

1 US ARMY ARDEC
AMSRD AAR AEM I
D CONWAY
BLDG 65N
PICATINNY ARSENAL NJ 07806-5000

NO. OF COPIES ORGANIZATION

1 US ARMY ARDEC
AMSTA DSA SA
A CLINE
BLDG 151
PICATINNY ARSENAL NJ 07806-5000

2 PM MAS
SFAE AMO MAS SMC
F HANZL
P RIGGS
BLDG 354
PICATINNY ARSENAL NJ 07806-5000

1 PM MAS
SFAE AMO MAS MC
G DEROSA
BLDG 354
PICATINNY ARSENAL NJ 07806-5000

1 AEROPREDICTION INC
F MOORE
9449 GROVER DR STE 201
KING GEORGE VA 22485

1 UNIVERSITY OF ILLINOIS
AERO ENG DEPT
J DUTTON
306F TALBOT LAB
104 S WRIGHT ST
URBANA IL 61801

2 ATK TACTICAL SYS DIV
ALLEGANY BALLISTICS LAB
D LEWIS
J OWENS
210 STATE RTE 956
ROCKET CENTER WV 26726

1 ATK ORDNANCE SYS
B BECKER
MN07 MW44
4700 NATHAN LN N
PLYMOUTH MN 55442

1 ALLIANT TECHSYSTEMS INC
C AAKUS
MN11 2830
600 SECOND ST NE
HOPKINS MN 55343

NO. OF COPIES ORGANIZATION

1 ATK
M JANTSCHER
MN07 LW54
5050 LINCOLN DR
EDINA MN 55436

3 ATK LAKE CITY
K ENLOW
D MANSFIELD
J WESTBROOK
PO BOX 1000
INDEPENDENCE MO 64051-1000

1 SCIENCE APPLICATIONS INTL CORP
J NORTHRUP
8500 NORMANDALE LAKE BLVD
STE 1610
BLOOMINGTON MN 55437

2 GOODRICH ACTUATION SYSTEMS
T KELLY
P FRANZ
100 PANTON RD
VERGENNES VT 05491

1 ARROW TECH ASSOC
W HATHAWAY
1233 SHELBURNE RD STE D8
SOUTH BURLINGTON VT 05403

1 KLINE ENGINEERING CO INC
R W KLINE
27 FREDON GREENDEL RD
NEWTON NJ 07860-5213

1 SIERRA BULLETS
P DALY
1400 W HENRY ST
SEDALIA MO 65302-0818

1 GEORGIA INST TECH
DEPT AEROSPACE ENGR
M COSTELLO
270 FERST ST
ATLANTA GA 30332

ABERDEEN PROVING GROUND

20 DIR USARL
RDRL WM
B FORCH
J SMITH
RDRL WMB
J NEWILL
M ZOLTOSKI
RDRL WMB A
D LYON
RDRL WMB C
I CELMINS
M CHEN
G COOPER
J DESPIRITO
F FRESCONI
B GUIDOS
K HEAVEY
B HOWELL
G OBERLIN
J SAHU
S SILTON
P WEINACHT
RDRL WMB D
C CANDLAND
J MORRIS
RDRL WMB F
W OBERLE

NO. OF
COPIES ORGANIZATION

2 DSTL BEDFORD
T BIRCH
B SHOESMITH
BLDG 115 RM 125
BEDFORD TECHNOLOGY PARK
BEDFORD
MK44 2FQ
UK

3 DEFENCE RESEARCH AND
DEVELOPMENT CANADA –
VALCARTIER
F LESAGE
D CORRIVEAU
N HAMEL
2459 PIE-XI BLVD NORTH
VAL-BELAIR (QC) G3J1X5
CANADA

INTENTIONALLY LEFT BLANK.